

The Clustering, Number Counts and Morphology of Extremely Red ($R - K > 5$) Galaxies to $K \leq 21$

Nathan D. Roche^{1,4}, Omar Almaini^{1,5}, James Dunlop^{1,6}, R.J. Ivison^{2,7}
and C.J. Willott^{3,8}

¹*Institute for Astronomy, University of Edinburgh, Royal Observatory, Edinburgh EH9 3HJ, Scotland.*

²*Astronomy Technology Centre, Royal Observatory, Edinburgh EH9 3HJ, Scotland.*

³*Astrophysics, Department of Physics, Keble Road, Oxford OX1 3RH, England.*

⁴ ndr@roe.ac.uk

⁵ omar@roe.ac.uk

⁶ jsd@roe.ac.uk

⁷ rji@roe.ac.uk

⁸ cjlw@astro.ox.ac.uk

11 February 2019

ABSTRACT

Using K and R band imaging of the ELAIS N2 field, we investigate the number counts, clustering, morphology and radio/X-ray emission of extremely red objects (EROs), defined as galaxies with $R - K > 5.0$. This criterion will select old, passive ellipticals at $z > 0.9$. To $K = 21$ we identify a total of 157 EROs in 81.5 arcmin^2 . The ERO number counts are lower than predicted by a pure luminosity evolution model, but higher than predicted by current Λ CDM-based hierarchical models. They can be fitted by a combination of moderate merging with a decrease with redshift in the comoving number density of passive galaxies.

We investigate the angular correlation function, $\omega(\theta)$, of the EROs, and find that the EROs have a much higher $\omega(\theta)$ amplitude (by almost an order of magnitude) than full K -limited samples of galaxies. These results, which are in agreement with Daddi et al. (2000), imply that the intrinsic clustering of EROs is stronger than that of present-day E/S0 galaxies. For our model’s cosmology and $N(z)$, we estimate the comoving correlation radius of EROs as $r_0 \simeq 16.6 \pm 3.7 h^{-1} \text{ Mpc}$.

We estimate seeing-corrected angular sizes and morphological types for a $K \leq 19.5$ subsample of EROs (31 galaxies) and find a $\sim 3:2$ mixture of bulge and disk profiles. Of these EROs $\sim \frac{1}{4}$ appear to be interacting, disturbed or otherwise irregular, and two are visible mergers. The angular sizes of the bulge-profile EROs are consistent with passively evolving ellipticals at the expected $z \sim 0.9\text{--}2$. Seven of the 31 bright EROs are detected as $F(1.4 \text{ GHz}) \geq 30 \mu\text{Jy}$ radio sources in a VLA survey. The strongest, at 5 mJy, is also a Chandra X-ray detection, and lies at the centre of a significant overdensity of EROs – it is probably an FRI radio galaxy in a $z \sim 1$ cluster. Of the other, much fainter, sources, five are point-like and may be weak AGN, while the sixth is elongated and aligned with the optical axis of an extended, low-surface brightness ERO, and hence probably a ULIRG-type starburst.

A possible interpretation is discussed in which the EROs are a mixture of (i) ‘pEROs’, strongly clustered passively evolving giant ellipticals, formed at high redshifts, and (ii) ‘dsfEROs’, less clustered, dusty, recent post-interaction galaxies, with a few active starbursts (ULIRGs). The pEROs are the oldest EROs and the dsfEROs are continually assimilated into to the ERO class, diluting the clustering and increasing the comoving number density. Both types ultimately evolve into today’s early-type galaxies.

Key words: galaxies: evolution; galaxies: elliptical and lenticular, cD; galaxies: high-redshift; radio continuum: galaxies

1 INTRODUCTION

Deep surveys at near-infra-red ($\sim 2 \mu\text{m}$) wavelengths revealed that a population of very red ($R - K > 5$ or $I - K > 4$,

Vega system) galaxies appears faintward of $K \sim 18$ (e.g. Elston et al. 1988; Hu and Ridgeway 1994). The colours and K magnitude range of these ‘extremely red objects’ (EROs)

are consistent with old, passive (i.e. no longer forming new stars) galaxies, observed at $z \sim 1$ or beyond. These would be the progenitors of present-day giant ellipticals, thought to have formed their stars at even higher ($z \geq 3$) redshifts.

The EROs are of great cosmological interest, as they will include the earliest formed of all galaxies, and their properties will help to answer the long-standing mysteries concerning the early evolution of elliptical galaxies (e.g. Jimenez et al. 1999). One hypothesis is that the present-day ellipticals formed in single starbursts at $z > 3$, thereafter undergoing only passive luminosity evolution, as in pure luminosity evolution (PLE) models, another is that they formed more recently through mergers of spiral galaxies, or by some combination of the two. Initial surveys of EROs (e.g. Barger et al. 1999) found fewer than expected from PLE models, and implied that ≤ 50 per cent of the local E/S0s could have formed in a single high-redshift starburst. However, the detection with SCUBA of many sub-mm sources, with optical magnitudes and colours consistent with dusty galaxies at $z > 2$, and $850\mu\text{m}$ fluxes indicative of star-formation rates (SFRs) as high as $\sim 1000M_{\odot}\text{yr}^{-1}$, provided strong evidence that some massive galaxies did form in intense early starbursts (e.g. Smail et al. 1999). The passive EROs could then be the intermediate stage between the SCUBA sources and local giant ellipticals.

With sufficient dust-reddening, high-redshift star-forming galaxies may also have $R - K > 5$. Spectroscopy of a few of the brightest EROs revealed that both old, passive (e.g. Dunlop et al. 1996; Spinrad et al. 1997; Stanford et al. 1997) and dusty starburst (e.g. Dey et al. 1999; Smith et al. 2001) galaxies were present, but the relative proportions remained uncertain.

The morphologies of the EROs provide further information on their nature. Moriondo, Cimatti and Daddi (2000) fitted radial profiles to WFPC2 and NICMOS images of 41 EROs (to $K \sim 21$) and estimated that 50–80 percent were elliptical-like and 15 percent irregular or interacting. Stiavelli and Treu (2000) studied 30 EROs to $H \sim 23$, using NICMOS, and classified these into E/S0, disk, irregular and point-like morphologies in a ratio 18:6:3:3. They assumed that only the first type were the progenitors of local E/S0s, and by comparing the counts of these with a PLE model (with $\Omega_m = 0.3$, $\Omega_{\Lambda} = 0.7$), estimated only ~ 15 per cent of the present-day number of E/S0s could have formed at $z \geq 3$.

Daddi et al. (2000) presented the first measurements of ERO clustering. They found the angular correlation function, $\omega(\theta)$, of $K \leq 19.2$ EROs to be almost an order of magnitude higher than that of all galaxies to the same K limit. As local giant ellipticals are intrinsically much more clustered than disk galaxies (e.g. Guzzo et al. 1997), this was interpreted as evidence that most EROs are $z > 1$ ellipticals.

Manucci et al. (2001) attempted a photometric separation of passive and dusty, star-forming EROs – hereafter pEROs and dsfEROs – on a plot of $J - K$ against $R - K$. Within a sample of 57 EROs with $K \leq 20$, they assigned equal numbers (21) to each class. Cimatti et al. (2002a) provided the first true measurement of the dsfERO/pERO ratio, identifying by spectroscopy approximately equal numbers (15 ‘dsf’, 14 ‘p’) amongst 45 EROs with $K \leq 19.2$. Firth et al. (2002) investigated ERO clustering to $H = 20.5$

($K \simeq 19.5$) and obtained similar results to Daddi et al. (2000).

In this paper we select a sample of $R - K > 5.0$ EROs from new K and R band images, investigate their number counts, clustering and morphologies and compare these results with evolutionary models. We do not yet have spectroscopy for these galaxies, but do have deep radio and X-ray observations which may identify starbursts and AGN. Magnitudes in this paper are given in the Vega system and can be converted to the AB system using $R_{AB} = R_{Vega} + 0.19$ and $K_{AB} = K_{Vega} + 1.87$. Quantities dependent on Hubble’s Constant are given in terms of $h_{50} = H_0/50$ or $h_{100} = H_0/100 \text{ km s}^{-1}\text{Mpc}^{-1}$.

This paper is organized as follows: Section 2 describes the dataset and its reduction and analysis, and Section 3 the selection of the EROs and their distribution on the sky. In Sections 4 and 5 we investigate, in turn, the number counts and angular correlation function, $\omega(\theta)$, of the $K \leq 21.0$ EROs and other galaxies, and compare with models. In Section 6 we fit radial profiles to a subsample of brighter, $K \leq 19.5$, EROs to investigate their morphologies and angular sizes, and in Section 7 describe the radio properties. Section 8 discusses these findings and with other recent studies of EROs, and their possible interpretation.

2 OBSERVATIONS

2.1 Data: K and R Imaging

Our K ($\lambda = 2.2\mu\text{m}$) and R band imaging covers an area within field N2 of the European Large Area ISO Survey (ELAIS, Oliver et al. 2001), centered at R.A. $16^{\text{h}}36^{\text{m}}30^{\text{s}}$ Dec $+41:04:30$. The first part of the K -band data consists of a mosaic of 16 contiguous fields observed using the UKIRT Fast-Track Imager (UFTI), on Mauna Kea, Hawaii, between 1 January and 31 May 2000. Most frames received a total of 8000 seconds exposure time. The UFTI camera contains a 1024×1024 pixel HgTeCd array which, with a pixel size of 0.091 arcsec, covers 1.55×1.55 arcmin.

The second part consists of three fields observed with the Isaac Newton Group Red Imaging Device (Ingrid) on the William Herschel Telescope (WHT), La Palma. The Ingrid fields lie on the edges of the UFTI mosaic, overlapping it slightly. Ingrid is fitted with a 1024×1024 pixel near-IR detector with a pixel size of 0.238 arcsec, covering 4.06×4.06 arcmin. Our Ingrid data are not quite as deep as the UFTI mosaic, due to a shorter exposure time (5540 sec) and lower instrumental sensitivity.

The UFTI and Ingrid observations lie within the area of an R -band image obtained with the Prime focus camera on the WHT (May 1999). This instrument contains 2 mosaiced 2048×4096 pixel EEV chips, with a pixel size of 0.238 arcsec, covering 16×16 arcmin. The R -band data, obtained in May 1999 as part of a study of faint Chandra X-ray sources (González-Solares et al. 2002), consists of 13 spatially dithered 600 sec exposures, combined to give an octagonal 16.4×16.9 arcmin frame with detection limit $R \simeq 26$. This has accurate astrometry (to ≤ 0.5 arcsec) based on the positions of radio sources.

This paper is based primarily on our UFTI and Ingrid data. However, in some sections – in particular the clustering

analysis – we also make use of galaxy catalogs from two European Southern Observatory Imaging Survey (EIS) fields. We downloaded the publically available detection catalogs for the EIS-DEEP AXAF and HDF2 fields, which are based on near-IR and optical imaging to a depth similar to our UFTI observations, from www.eso.org. The AXAF catalog covers 45.2 arcmin^2 in both K and R . The HDF2 catalog covers 28.2 arcmin^2 in K , but with R imaging in only a 11.9 arcmin^2 subregion.

2.2 Radio/X-ray/sub-mm Data

The ELAIS N2 field has been surveyed in a number of other passbands. Radio (VLA) observations (Ivison et al. 2002) reach a 3σ detection limit of $F(1.4 \text{ GHz}) = 30\mu\text{Jy}$ (with beam size $1.40 \times 1.46 \text{ arcsec}$), and detect > 100 sources. The available X-ray data consist of a 75ks Chandra observation made on 2 August 2000, covering a $16.9 \times 16.9 \text{ arcmin}$ field, in which 91 sources were detected to $F(0.5\text{--}8.0\text{keV}) \simeq 6 \times 10^{-16} \text{ ergs s}^{-1}\text{cm}^{-2}$ (Manners et al. 2002; Almaini et al. 2002), most of which now have optical identifications (González-Solares et al. 2002). Sub-mm observations with SCUBA, detected 17 sources above a 3.5σ limit $F(850\mu\text{m}) \simeq 8 \text{ mJy}$ (Scott et al. 2002).

2.3 Data Reduction

The UFTI and Ingrid data were reduced and analysed using IRAF. The UFTI dataset was made up of 16 pointings, each observed for 9 spatially dithered exposures of 800 sec (two pointings had slightly different exposures of 700 sec and 1100 sec and were renormalized to 800 sec). Our intention was to combine all $9 \times 16 = 144$ exposures into a single mosaiced image, and to this end, the spacing between the grid of pointings had been matched to the field-of-view and dither pattern so that the resulting mosaic would have an approximately uniform 7200 sec coverage (except at the edges).

The sky background was subtracted from all UFTI data (using IRAF ‘sky’). Astrometry was derived for each pointing, by reference to detections on the WHT R image. However, even with these transforms, the raw exposures could not be mosaiced with acceptable accuracy, indicating slight rotations or other distortions between them. This problem was remedied by choosing one pointing as a reference and then using IRAF ‘wcsmap’ to fit a general polynomial transform between its co-ordinate system and that of the other 15. These 15 frames were then rebinned, using IRAF ‘geotran’, into the co-ordinate system of the reference. The rebinned data could then be simply combined, using IRAF ‘combine’ (with ‘offsets=wcs’), into a 16-frame UFTI mosaic (taking care to exclude any ‘bad’ regions from each exposure in the summation). The final step was to trim the noisy edges (which received less than the full exposure time) from the mosaic, to leave a total usable area of 38.7 arcmin^2 .

The three fields of Ingrid data overlap slightly with the UFTI mosaic, but not with each other, and were reduced separately. The data for each field consisted of 90 spatially dithered exposures of 61.56 seconds (each in turn made up of 6 exposures which were co-added during observing). All exposures were debiased, and flat-fielding was performed for

blocks of 9 consecutive exposures, by dividing them by their median image (derived using ‘combine’ with sigclip rejection, and normalized to a mean of unity).

The spatial dithers, which followed the same sequence for each block of 9 exposures, were measured using ‘xregister’. All 90 exposures of each of the three fields could then be added using ‘combine’. Magnitude calibration was determined from short exposures of UKIRT standard stars, interspersed with the observations. We then matched $\sim 10\text{--}15$ stars on each Ingrid field (detected as described below) to their known RA and Dec on the WHT R image and fitted astrometric transforms using IRAF ‘pltsol’ (with rms residuals $0.11\text{--}0.25 \text{ arcsec}$).

2.4 Source Detection

Sources were detected on the K and R images using SExtractor (Bertin and Arnouts 1996). Throughout, magnitudes given for the detections are the ‘total’ magnitudes derived by SExtractor by fitting elliptical apertures to each source.

For the UFTI mosaic, we adopted a detection criterion that a source must exceed a $1.5\sigma_{sky}$ threshold ($21.36 \text{ K mag arcsec}^{-2}$) in 16 contiguous pixels (0.13 arcsec^2), and also used a detection filter of Gaussian FWHM 4 pixels. Using a plot of detection magnitude against FWHM, stars could be separated from galaxies to $K = 16.5$ and many spurious noise detections could be rejected. The mean FWHM of unsaturated stars was only 0.67 arcsec , indicating very good seeing, although there is significant variation in the PSF between the different frames of the mosaic.

For the WHT R -band image the adopted detection threshold was $1.5\sigma_{sky}$ ($26.66 \text{ R mag arcsec}^{-2}$) in a minimum area 4 pixels (0.23 arcsec^2), with a detection filter of 2.0 pixels Gaussian FWHM. The total usable area is 212 arcmin^2 . The mean stellar FWHM is 0.76 arcsec , and from the number count of detected galaxies, detection appears to be complete to $R \simeq 25.5$, with moderate (25–30 per cent) incompleteness at $25.5 < R < 26$ and a turnover at $R > 26$. The Ingrid data (total area 49.5 arcmin^2) have a similar pixel size and again we used the detection criterion of $1.5\sigma_{sky}$ ($20.60\text{--}20.65 \text{ R mag arcsec}^{-2}$) in ≥ 4 pixels, with a Gaussian 2.0 pixel FWHM filter. Stars (45) were separated from galaxies to $K = 16.5$. The mean stellar FWHM of 0.68 arcsec again indicated good seeing. The galaxy counts from the Ingrid data are very similar to the UFTI counts to $K = 19.5$ but turn over at $K > 20$ rather than at $K > 21$, hence are $\sim 1 \text{ mag}$ less deep.

The next step was to merge the Ingrid and UFTI catalogs, by flagging for exclusion the Ingrid detections within the area already covered by the UFTI mosaic. The Ingrid and UFTI magnitudes of the overlap-region objects were generally consistent within $\sim 0.1 \text{ mag}$. Excluding overlaps reduced the total catalog area to 83.6 arcmin^2 . Hereafter we make use of the combined UFTI+Ingrid catalog to $K = 20$ and the UFTI mosaic only at $20 < K < 21$.

3 IDENTIFYING THE $R - K > 5$ GALAXIES

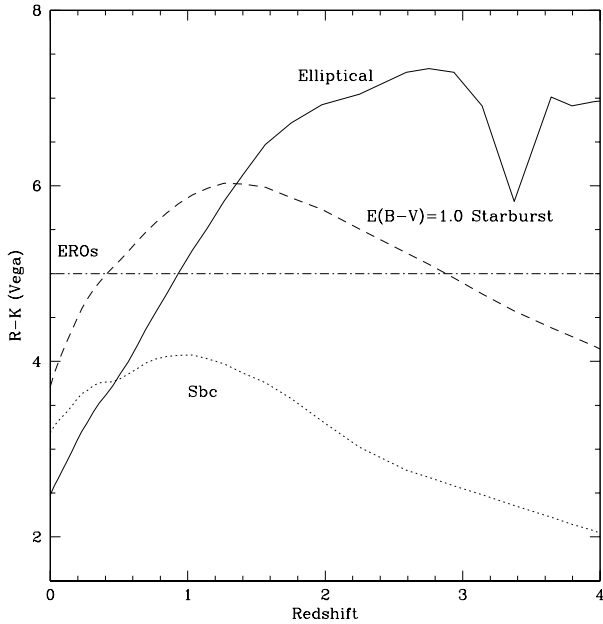


Figure 1. Observed $R-K$ colour against redshift, for three models representing an evolving elliptical galaxy (pERO), a heavily reddened starburst (dsfERO), and a normal spiral (which is never an ERO).

3.1 The Significance of $R-K > 5$

Galaxies with observer-frame $R-K > 5.0$ ($R-K > 3.31$ in the AB system) are either old, passive (zero or near-zero SFR) galaxies at $z \geq 0.9$, or are very dust-reddened. Figure 1 shows $R-K$ against redshift for three models, computed using Pegase2 (Fioc and Rocca-Volmerange 1997) with the time-redshift relation for $\Omega_m = 0.3$, $\Omega_\Lambda = 0.7$ and $h_{100} = 0.55$.

(i) An evolving model representing an elliptical galaxy, which forms stars in a 1 Gyr dust-reddened burst at $z > 3.4$. The SFR and dust then fall to zero, and passive evolution occurs. The galaxy would have $R-K > 5.0$ at all $z > 0.93$ and hence is a ‘pERO’.

(i) A pure, non-evolving starburst, with very strong dust reddening of $E(B-V) = 1.0$ mag. Such ‘dsfEROs’ are reddest at $1 < z < 1.6$, but if as dusty as this model can be EROs at all $0.5 < z < 3$. Starburst galaxies with an old stellar component, or post-starbursts, could be EROs with somewhat less reddening.

(iii) For comparison, a model representing an evolving spiral (Sbc) with near-solar metallicity and a ‘normal’ amount of dust. ‘Normal’ star-forming spirals like this do not have $R-K > 5$ at any redshift.

3.2 ERO Selection

The K -detected galaxies were matched in RA and Dec with detections on the WHT R -band image (two small areas of Ingrid data were not covered in R , slightly reducing the $K+R$ overlap region to 81.5 arcmin^2). The R detection closest to the centroid of each K detection was taken to be the correct counterpart, out to a maximum offset of 2.5 arcsec, although

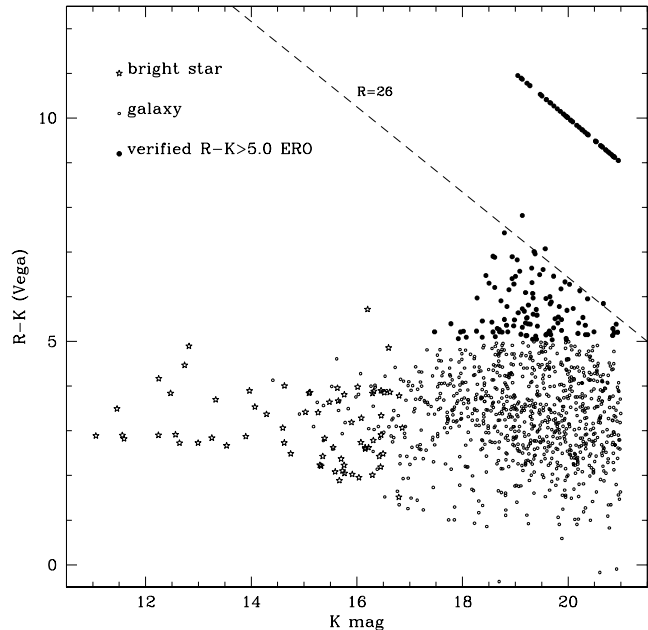


Figure 2. $R-K$ colour against K for UFTI and Ingrid detections to $K = 21$, with star-galaxy separation to $K = 16.5$. Galaxies undetected in R , and hence included as EROs, are placed at $R = 30$, but may lie on or anywhere above the $R = 26$ locus.

most matches were to ≤ 0.5 arcsec. Any K detection with $K \leq 21$ and either $R-K > 5$ or no R counterpart was flagged as a candidate ERO.

The K detections in the latter category are either (i) spurious, (ii) real galaxies where the R counterpart is obscured (e.g. by a diffraction spike) or merged with a brighter detection, (iii) real galaxies with very faint R magnitudes, almost certainly $R > 26$, which can be reasonably be classified as EROs. All were carefully examined by eye, on the K image and at the corresponding position on the R image. In this way, a number of spurious detections were identified, and thereafter excluded.

Our final catalog of verified EROs consists of 157 objects (including 47 undetected in R), of which 98 are on the UFTI mosaic. Figure 2 shows $R-K$ against K magnitude for the detected galaxies – EROs appear only at faint magnitudes, mostly $K > 18$. One much brighter ($K = 16.2$) object has $R-K = 5.72$, but appears stellar and is almost certainly a red Galactic star, and is not included here as an ERO.

In the same way, the K band detections in the EIS catalogs were matched by RA/Dec co-ordinates to their counterparts in the R catalogs. Stars were separated from galaxies on the basis of a ‘stellarity parameter’ exceeding 0.85. Galaxies with $K \leq 21$ and $R-K > 5.0$ on the AXAF field (83) and the KR overlap of the HDF2 field (41) were flagged as EROs.

3.3 Spatial Distribution

Figures 3 and 4 shows the distribution of EROs on the UFTI+Ingrid and the EIS AXAF and HDF2 fields. ERO

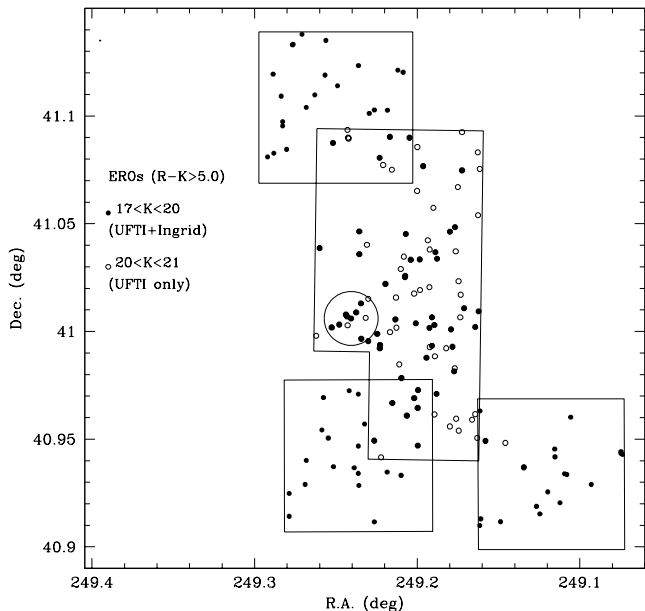


Figure 3. Distribution on the sky of the $K \leq 20$ EROs ($R - K > 5.0$) on the UFTI mosaic (central area) and the 3 Ingrid fields, with the $20 < K < 21$ EROs on the UFTI field only. The plotted circle shows a 45 arcsec radius around UFTI detection 608.

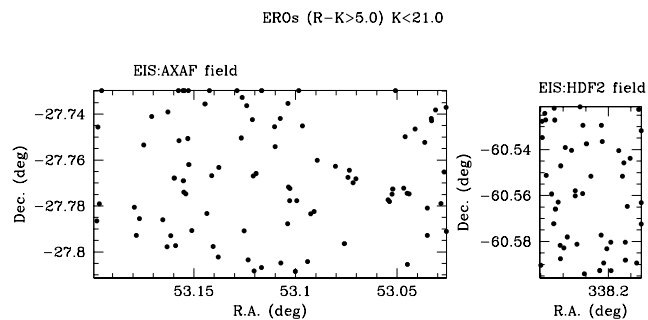


Figure 4. Distribution on the sky of the $K \leq 21$ EROs ($R - K > 5.0$) on the EIS catalogs of the AXAF field and the area of the HDF2 field covered in both K and R .

maps are useful for identifying galaxy clusters at $z \geq 1$, where the early-type members will show up as an arcmin-scale overdensity (e.g. Stanford et al. 1997). In our data, there may be a group of EROs centered on UFTI detection number 608, a bright ERO ($K = 17.78$) of particular interest in that it is a radio and X-ray source (Section 7). Within a 45 arcsec radius (shown on Figure 3) of its position there are 8 EROs with $K \leq 20$, compared to 2.4 expected for a random distribution. These EROs are discussed further in Section 6.3.

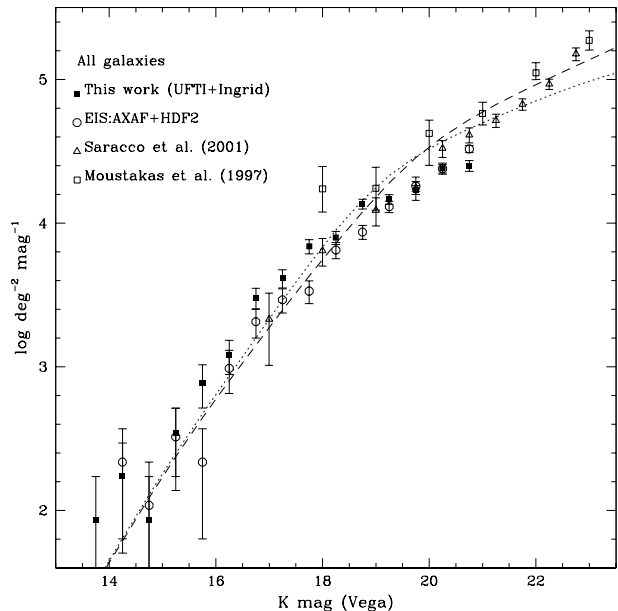


Figure 5. K -band differential galaxy number counts, for galaxies of all colours, from our data (Ingrid+UFTI to $K = 20$, UFTI only at $20 < K < 21$), the two EIS fields, and the deeper surveys of Moustakas et al. (1997) and Saracco et al. (2001), compared with two models; PLE (dotted), merging with $R_\phi = R_{m^*} = 0.3$ (dashed).

4 NUMBER COUNTS OF GALAXIES AND EROS

4.1 Observations

Figure 5 shows K -band differential number counts for all galaxies, from the combined UFTI+Ingrid data at $K \leq 20$ and UFTI data only at $20 < K < 21$. Also shown are counts from the two EIS fields (combined), and the deeper (to $K \sim 23$) Keck and ESO-VLT surveys of Moustakas et al. (1997) and Saracco et al. (2001). These are reasonably consistent, although both UFTI+Ingrid and AXAF+HDF2 counts are slightly low at $K \geq 20$, suggesting some incompleteness – the ratio of the UFTI+Ingrid all-galaxy count to that of Saracco et al. (2001) falls from 0.968 at $19.5 < K < 20.0$ to 0.725 at $20.0 < K < 20.5$ and 0.611 at $20.5 < K < 21.0$.

Figure 6 and Table 1 show number counts for EROs only. The fraction of EROs in the UFTI+Ingrid data is $112/812 = 13.8$ per cent at $K \leq 20$ and $157/1076 = 14.6$ per cent at $K \leq 21.0$. The ‘incompleteness corrected’ count is derived by dividing our observed ERO count by the ratio of our count for all galaxies to that of Saracco et al. (2001) at the same K limit. We also plot the ERO counts from Daddi et al. (2000), which are also selected as $R - K > 4$, and from Saracco et al. (2001) – but note that these are selected with a different criterion of $J - K > 1.9$, which may include a greater number of ‘dsFEROs’. The UFTI+Ingrid ERO counts agree well with these two previous surveys, while the ERO counts from the EIS fields are slightly lower at $K < 20$ but very similar at $K = 20$ –21.

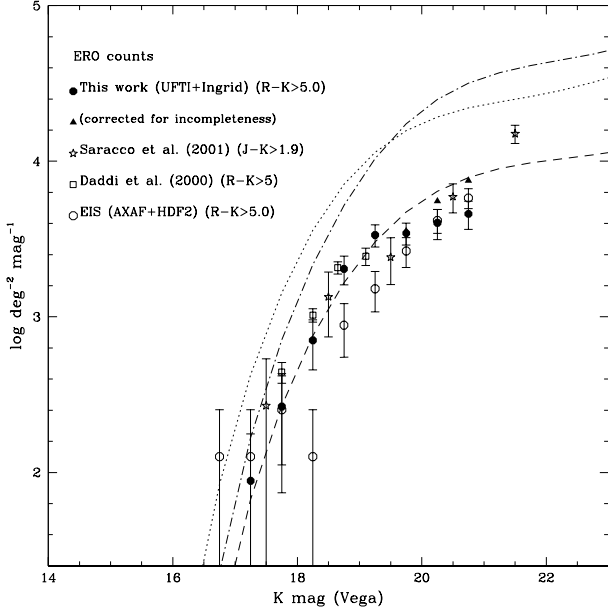


Figure 6. K -band differential galaxy number counts for $R-K > 5.0$ EROs from our UFTI+Ingrid data, the EIS fields and Daddi et al. (2000), and for $J-K > 1.9$ EROs in Saracco et al. (2001), with minimal \sqrt{N} errors, compared with $R-K > 5.0$ galaxy counts predicted by PLE (dotted), merging with $R_\phi = R_m = 0.3$ (dot-dash), and ‘M-DE’ merging with $R_m = 0.3$ $R_\phi = -0.46$ (dashed) models.

Table 1. Observed number counts (number N_g and surface density, ρ) of $R-K > 5.0$ EROs on the UFTI+Ingrid field, with \sqrt{N} errors, and (at $K > 19.5$) ρ with an estimated incompleteness correction.

K interval	N_g	ρ (Obs.) deg $^{-2}$ mag $^{-1}$	ρ (‘Corrected’) deg $^{-2}$ mag $^{-1}$
17.0–17.5	1	88.4 \pm 88.4	-
17.5–18.0	3	256.0 \pm 153.0	-
18.0–18.5	8	706.8 \pm 249.9	-
18.5–19.0	23	2032.2 \pm 423.7	-
19.0–19.5	38	3357.5 \pm 544.7	-
19.5–20.0	39	3445.9 \pm 551.8	3560.
20.0–20.5	21	4018.6 \pm 876.9	5543.
20.5–21.0	24	4592.6 \pm 937.5	7517.

4.2 Models: PLE and Merging

These counts are compared with simple galaxy evolution models, with and without the effects of merging. All models used here assume $\Omega_M = 0.3$, $\Omega_\Lambda = 0.7$, and are based on the observed K -band galaxy luminosity functions (from 2MASS) of Kochanek et al. (2001). The luminosity evolution is modelled using Pegase2 (Fioc and Rocca-Volmerange 1997) with a range of star-formation histories, and (as in Roche et al. 2002), an initial mass function with the Salpeter slope $x = 2.35$ (where $\frac{dN}{dM} \propto M^{-x}$) at $0.7 < M < 120 M_\odot$, flattening to $x = 1.3$ at $0.1 < M < 0.7 M_\odot$.

Galaxies in the early-type luminosity function (represented as a Schechter function with $M_K^* = -25.04$, $\alpha =$

-0.92 $\phi^* = 0.0005625 \text{ Mpc}^{-3}$ for $h_{50} = 1$) form all their stars in an initial dust-reddened ($E(B-V) = 0.65 \text{ mag}$) burst, beginning 16 Gyr ago ($z \simeq 6$), with a range of durations represented as either 1 Gyr (for half) or 2 Gyr. After the burst both dust and SFR fall to zero and evolution is thereafter passive. Galaxies in the late-type luminosity function ($M_K^* = -24.49$, $\alpha = -0.87$ $\phi^* = 0.0012625 \text{ Mpc}^{-3}$ for $h_{50} = 1$) are represented with a range of continuous star-formation models with different timescales and moderate amounts of dust. The only $R-K > 5$ galaxies in this model are the E/S0s at $z > 0.93$.

In the pure luminosity evolution (PLE) model the galaxies evolve only in L^* , with no change in ϕ^* or α . The merging model assumes the same luminosity evolution but superimposed on this is an increase in comoving number density (ϕ^*) with redshift, and an associated decrease in the characteristic galaxy mass (m^*) and luminosity (L^*).

We parameterize the merger rate in terms of the effect of merging on galaxy mass, $\frac{\Delta(m^*)}{m^*} = R_m(z)$ per Hubble time (t_H). Observationally, Patton et al. (2001) estimated from CNOC2 data that $R_m(z) \simeq 0.3(1+z)^{2.3}$ to $z = 0.55$. If we assume this evolution to continue to $z = 1$, with $R_m(z)$ constant at $z \geq 1$, then $m^*(z)$ will evolve as:

$$\frac{dm^*}{dt} = m_z^* R_m(0) t_H^{-1} (1+z)^{2.3} \quad \text{at } z < 1$$

$$\frac{dm^*}{dt} = m_z^* R_m(0) t_H^{-1} 2^{2.3} \quad \text{at } z \geq 1$$

approximating the lookback time $t_{\text{now}} - t \simeq t_H - t_H(1+z)^{-1}$, gives $\frac{dt}{dz} = -t_H(1+z)^{-2}$. Substituting,

$$\frac{dm^*}{dz} = -m_z^* R_m(0) t_H^{-1} (1+z)^{0.3} \quad \text{at } z < 1$$

$$\frac{dm^*}{dz} = -m_z^* R_m(0) t_H^{-1} 2^{2.3} (1+z)^{-2} \quad \text{at } z \geq 1$$

Integrating,

$$\int_0^z \frac{dm^*}{dz} = R_m(0) \int_0^z (1+z)^{0.3} dz$$

$$\ln m^*(z) = \ln m^*(0) - R_m(0) \frac{(1+z)^{1.3} - 1}{1.3}$$

$$m^*(z) = m^*(0) \exp[-R_m(0) \frac{(1+z)^{1.3} - 1}{1.3}] \quad z < 1$$

and,

$$\int_1^z \frac{dm^*}{dz} = 2^{2.3} R_m(0) \int_1^z (1+z)^{-2} dz$$

$$\ln m^*(z) = \ln m^*(1) - 2^{2.3} R_m(0) \left(\frac{1}{2} - (1+z)^{-1} \right)$$

$$m^*(z) = m^*(1) \exp[-2^{1.3} R_m(0) (1 - 2(1+z)^{-1})] \quad \text{at } z \geq 1$$

with $R_m(0) = 0.3$ this gives $m^*(1, 2, 3) = (0.714, 0.558, 0.493)m^*(0)$. If the corresponding opposite evolution in comoving number density, R_ϕ , occurs at the same rate ($R_\phi = R_m$), galaxies at $z \sim 3$ are half as bright but twice as numerous as they would be in a PLE model.

As shown on Figure 5, the model counts for full K -limited samples are relatively insensitive to merging, and the

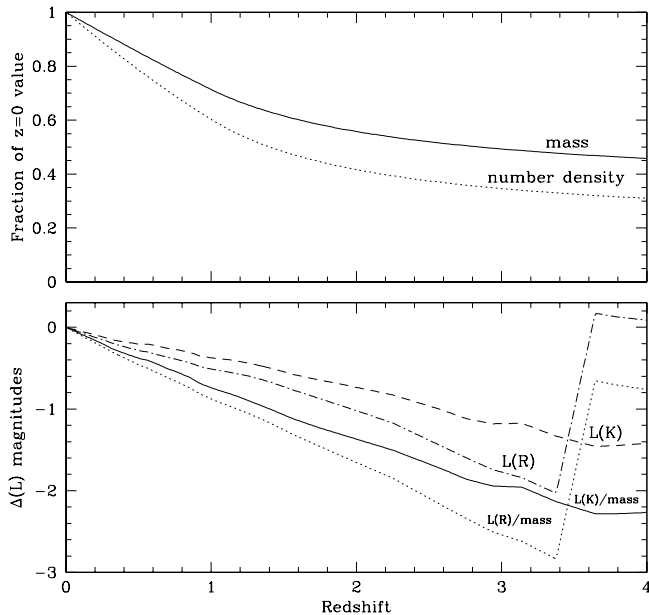


Figure 7. Features of the ‘M-DE’ model; (above) evolution of characteristic galaxy mass m^* and comoving number density ϕ^* ; (below) evolution of the characteristic luminosity L^* , in the rest-frame K and R bands, and of the luminosity per unit mass, for an elliptical with a 1 Gyr initial starburst (star-formation at $3.4 < z < 6$).

observations – considering the uncertainties in L^* evolution and luminosity functions – do not distinguish between the plotted models. On Figure 6 the same models are used to predict the counts of $R - K > 5.0$ EROs. Although only the ‘pERO’ type is included, the PLE model overpredicts the ERO counts at all magnitudes, by factors ~ 3 . The inclusion of $R_\phi = R_m = 0.3$ merging improves the fit at the bright end, but increases the overprediction at $K > 20$.

If we retain $R_m = 0.3$ and vary R_ϕ to best-fit our incompleteness-corrected ERO count, χ^2 is minimized for $R_\phi \approx -0.46$ (with error bar ± 0.10). This model, hereafter ‘M-DE’ (merging with negative density evolution), is plotted and clearly gives a better fit. Figure 7 illustrates the features of this model. Both mass and comoving number density decrease with redshift. Luminosity per unit mass (shown for restframe R and K) increases with redshift due to passive evolution (at $z > 3.4$ the galaxy is starbursting and most of the red light is hidden by dust). Luminosity (L^*) increases with z at a slower rate as it is partially cancelled by the decrease in mass. Physically, this model could be represented as 60 percent of the present-day comoving number density of E/S0 galaxies forming at $z > 1$, and 42 percent at $z > 2$, with the remainder originating at lower redshifts, e.g. from mergers of disk galaxies in which the remaining gas content is exhausted in a merger-triggered starburst. Some spiral-to-elliptical transformation could also occur through the cumulative effect of non-merging interactions, or gas-stripping in clusters.

In addition to rejecting the PLE model, the ERO counts do not support the other extreme case of ‘pure’ hierarchical merging. Cimatti (2002b) compares the observed count of

passive EROs at $K \leq 19.2$ with the predictions of two such models from Firth et al. (2002) and Smith et al. (2002), both derived from Λ CDM cosmologies. These models predict, respectively, 0.19 and 0.04 EROs arcmin $^{-2}$ at $K \leq 19.2$. Our observed (UFTI+Ingrid) count of EROs to this limit is 0.60 ± 0.09 arcmin $^{-2}$, and hence a mixture of formation histories, as represented by the M-DE model, is preferred.

5 CLUSTERING OF EROS

5.1 Calculating the Angular Correlation Function

The clustering properties of the EROs may provide clues to their nature and history. We calculate the angular correlation function, $\omega(\theta)$ (see e.g. Roche and Eales 1999) for the UFTI+Ingrid fields (UFTI only at limits $K > 20$) and for the two EIS fields, for both $R - K > 5$ galaxies and full K -limited samples, as described below.

For N_g galaxies brighter than a chosen magnitude limit, there will be $\frac{1}{2}N_g(N_g - 1)$ possible galaxy-galaxy pairs. These are counted in bins of separation of width $\Delta(\log \theta) = 0.2$, giving a function $N_{gg}(\theta_i)$. A large number of random points ($N_r = 50000$ here) is scattered over the same area as covered by the real galaxies, and the separations of the $N_g N_r$ galaxy-random pairs, taking the real galaxies as the centres, are counted in bins to give $N_{gr}(\theta_i)$. The separations of the $\frac{1}{2}N_r(N_r - 1)$ random-random pairs are also counted to give $N_{rr}(\theta_i)$.

If $DD = N_{gg}(\theta_i)$, and DR and RR are the galaxy-random and random-random counts normalized to have the same summation over θ ,

$$DR = \frac{(N_g - 1)}{2N_r} N_{gr}(\theta_i)$$

$$RR = \frac{N_g(N_g - 1)}{N_r(N_r - 1)} N_{rr}(\theta_i)$$

then, using the Landy and Szalay (1993) estimator,

$$\omega(\theta_i) = \frac{DD - 2DR + RR}{RR}$$

Errors were estimated by dividing the data area into 20 sub-areas and then recalculating $\omega(\theta)$ for 20 subsamples, each time excluding both the real galaxies and the random points from a different sub-area and using the remaining 19. The scatter between the $\omega(\theta)$ of these 20 subsamples is then multiplied by $\sqrt{\frac{19 \times 19}{20}} = 4.25$ to give the error bars for the full dataset $\omega(\theta)$.

This estimate will be negatively offset from the true $\omega(\theta)$ due to the restricted area of observation (the ‘integral constraint’). If the real $\omega(\theta)$ is of the form $A_\omega \theta^{-\delta}$, where A_ω is an amplitude, the estimate corresponds to $A_\omega(\theta^{-\delta} - C)$. The negative offset AC can be estimated by doubly integrating an assumed true $\omega(\theta)$ over the field area Ω ,

$$AC = \frac{1}{\Omega^2} \iint \omega(\theta) d\Omega_1 d\Omega_2$$

Using the random-random correlation, this can be done numerically –

$$C = \frac{\sum N_{rr}(\theta) \theta^{-\delta}}{\sum N_{rr}(\theta)}$$

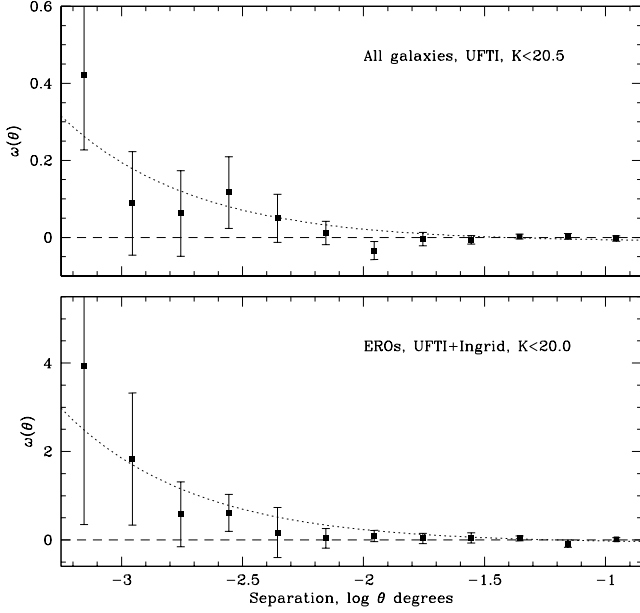


Figure 8. Angular correlation functions, $\omega(\theta)$ as calculated for all galaxies on the UFTI field to $K < 20.5$, and the EROs on the UFTI+Ingrid field to $K < 20.0$, with best-fit functions of the form ‘ $A_\omega(\theta^{-0.8} - C)$ ’ (dotted).

Assuming $\delta = 0.8$, this gives $C = 9.226$ for the combined UFTI+Ingrid area, 13.46 for the UFTI mosaic only, 12.71 for the AXAF field, and for HDF2, 17.45 for the K -band area and 21.72 for the subregion covered in $K + R$.

The amplitude A_ω is then obtained by least-squares fitting $A(\theta^{-0.8} - C)$ to the observed $\omega(\theta)$, over the range $1.26 < \theta < 502$ arcsec ($1.26 < \theta < 317$ arcsec for the HDF2 field), weighting each point using the error bars estimated as above. To estimate an error on A_ω , the same function is then fitted to the $\omega(\theta)$ of each of the 20 subsamples, and multiplying the scatter between the subsample A_ω by, again, 4.25.

5.2 $\omega(\theta)$ results

Figures 8 and 9 show the observed $\omega(\theta)$, with the fitted functions, at four K -band limits. Table 2 gives $\omega(\theta)$ amplitudes separately for the UFTI+Ingrid and EIS fields. Evidently, for single fields of this size, the detection of clustering is at best marginal. With the aim of improving the significance, we combine the three A_ω by averaging with each field weighted by N_{gal} . The error bars are combined as $[\sum(\text{error bar})^{-2}]^{-0.5}$. The combined A_ω , representing total areas between 94 and 156 arcmin², are given in Table 2 and plotted on Figures 10 and 11.

For full K -limited samples, our A_ω results are consistent with previous studies. The EROs appear to be much more clustered, by almost an order of magnitude, than the full sample. Our ERO A_ω is consistent with Daddi et al. (2000), if their scaling is extrapolated to $K = 21$.

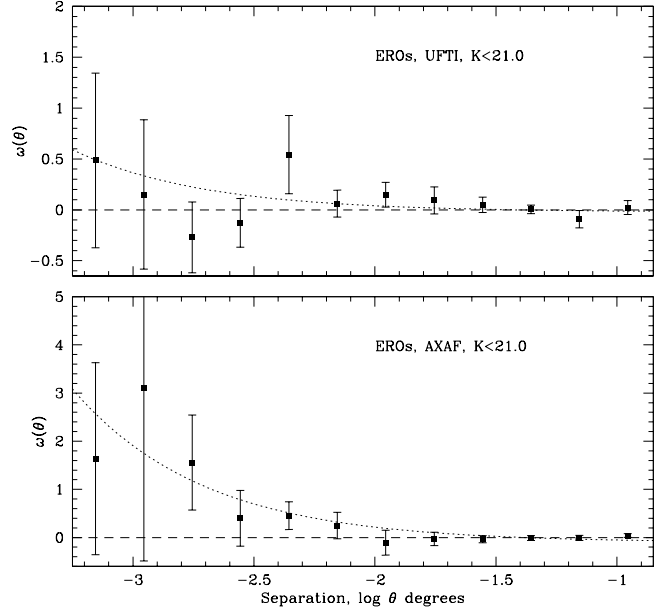


Figure 9. As Figure 8 for EROs on the UFTI and AXAF fields to $K < 21.0$.

5.3 Modelling and Interpretation of $\omega(\theta)$

The observed A_ω depends on the redshift distribution $N(z)$ and the cosmological geometry (through the angular size distance), as well as the intrinsic 3D correlation function of the galaxies $\xi(r, z)$. To interpret A_ω , we begin by modelling $N(z)$, for all galaxies and for EROs, for both PLE and M-DE. Figure 12 shows the ERO model $N(z)$ at $K \leq 19.5$ and $K \leq 21.0$. The M-DE model is lower in normalization and also less extended in redshift, especially at the brighter limit.

The intrinsic (three-dimensional) clustering of galaxies is represented here by the simplified form

$$\xi(r, z) = (r/r_0)^{-1.8}(1+z)^{-(3+\epsilon)}$$

where r_0 is the correlation radius and ϵ represents the evolution with redshift, $\epsilon = 0$ being clustering stable in proper coordinates, and $\epsilon = -1.2$ comoving clustering. This produces a projected (two-dimensional) clustering, $\omega(\theta) = A_\omega \theta^{-0.8}$, where the amplitude A_ω is given by Limber’s formula (see e.g. McCracken et al. 2001),

$$A = C_\gamma r_0^{1.8} \int_0^\infty \frac{(1+z)^{-(3+\epsilon)}}{d_A^{0.8}(z) \frac{dr(z)}{dz}} [(N(z)^2) dz] / [\int_0^\infty N(z) dz]^2$$

where $d_A(z)$ is the angular diameter distance, $r(z)$ is proper distance and $C_\gamma = 3.679$ for a $r-1.8$ power-law.

Table 2. Galaxy $\omega(\theta)$ amplitudes A_ω (in units of 10^{-4} at one degree) of full K -limited galaxy samples and of EROs ($R - K > 5.0$), as estimated from UFTI+Ingrid data (UFTI only at $K > 20$), for the EIS HDF2 and AXAF catalogs, and for all these combined (see text). N_g is the number of galaxies in each sample.

(i) All galaxies

K mag limit	UFTI+Ingrid		HDF2		AXAF		Combined
	N_g	A_ω	N_g	A_ω	N_g	A_ω	A_ω
19.00	444	8.76 ± 6.50	85	46.94 ± 18.32	149	39.20 ± 20.99	20.24 ± 5.88
19.25	524	9.84 ± 5.43	99	42.63 ± 15.94	187	35.45 ± 14.39	19.75 ± 4.84
19.50	615	9.30 ± 5.26	120	31.87 ± 14.96	234	25.44 ± 10.14	15.99 ± 4.72
19.75	714	5.32 ± 4.48	143	29.14 ± 13.36	282	16.30 ± 7.68	11.03 ± 3.71
20.00	813	5.76 ± 3.65	181	19.43 ± 8.32	340	8.07 ± 6.01	8.20 ± 2.93
20.25	418	8.24 ± 4.93	224	12.32 ± 5.61	406	4.62 ± 4.48	7.71 ± 2.85
20.50	486	6.77 ± 3.56	265	2.02 ± 6.78	477	0.15 ± 3.84	3.17 ± 2.44
20.75	547	5.83 ± 3.03	322	1.56 ± 3.91	571	0.37 ± 3.02	2.71 ± 1.88
21.00	622	3.30 ± 2.86	386	-2.69 ± 2.94	659	-0.22 ± 2.58	0.52 ± 1.61

(ii) $R - K > 5.0$ galaxies

K mag limit	UFTI+Ingrid		HDF2		AXAF		Combined
	N_g	A_ω	N_g	A_ω	N_g	A_ω	A_ω
19.00	35	392.2 ± 280.9	5	23.29 ± 891.0	7	306.7 ± 750.6	327.9 ± 162.3
19.25	56	226.9 ± 151.0	6	90.85 ± 287.9	15	331.7 ± 410.6	263.8 ± 129.2
19.50	73	151.2 ± 59.2	7	84.04 ± 230.1	17	327.1 ± 296.4	193.7 ± 56.6
19.75	93	86.63 ± 35.26	8	-42.34 ± 188.6	21	159.7 ± 163.0	98.48 ± 34.16
20.00	112	76.61 ± 33.25	12	-92.28 ± 71.76	33	91.68 ± 63.87	69.23 ± 28.95
20.25	63	36.02 ± 24.29	15	-38.34 ± 66.05	45	123.7 ± 95.26	64.56 ± 22.27
20.50	74	10.95 ± 22.76	20	19.5 ± 64.80	58	103.6 ± 75.90	50.44 ± 14.31
20.75	83	10.51 ± 14.73	29	-22.28 ± 48.43	71	79.45 ± 49.86	34.48 ± 13.22
21.00	98	15.34 ± 14.73	41	-16.79 ± 19.73	83	67.26 ± 36.00	30.75 ± 11.28

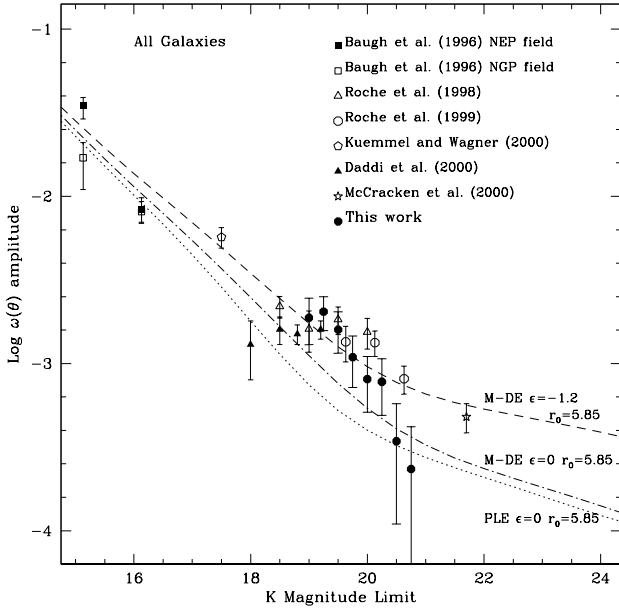


Figure 10. The scaling of $\omega(\theta)$ amplitude with K magnitude limit, for full K -limited samples of galaxies, as derived from our data (UFTI+Ingrid and HDF2 and AXAF fields combined), and previously published K -band $\omega(\theta)$. Three models are shown, all with $\Omega_M = 0.3$ $\Omega_\Lambda = 0.7$ and $r_0 = 5.85h_{100}^{-1}$ Mpc; PLE with $\epsilon = 0$ (dotted), M-DE with $\epsilon = 0$ (dot-dash) and M-DE with $\epsilon = -1.2$ (dashed).

Figure 10 shows three models for the $\omega(\theta)$ scaling of full K -limited samples. All assume $r_0 = 5.85h_{100}^{-1}$ – the normalization estimated by Cabanac, de Lapparent and Hickson (2000) from an I -limited survey – and a $\Lambda = 0.3$ cosmology. Of these models the uppermost ($\epsilon = -1.2$) appears the closest to observations, but this does not necessarily imply that the clustering is comoving. Giant ellipticals are particularly strongly clustered – e.g. Guzzo et al. (1987) estimate $r_0 = 8.35 \pm 0.75h_{100}^{-1}$ Mpc for E/S0 galaxies with $M_B < -21$ ellipticals – and likely to be more prominent in K -band than I -band surveys, so a slightly larger r_0 might be appropriate for this passband.

On the basis that the EROs will be mostly giant ellipticals, we first model their clustering with $r_0 = 8.35h_{100}^{-1}$ Mpc (Figure 11) However, the observed ERO clustering is significantly above this model, even with $\epsilon = -1.2$. If we assume the M-DE model with $\epsilon = -1.2$, and vary r_0 , the χ^2 for our $\omega(\theta)$ results is minimized for $r_0 = 16.6 \pm 3.7h_{100}^{-1}$. This model is also reasonably consistent with the results of both Daddi et al. (2000) and Firth et al. (2002).

This implies that EROs, to at least $K = 21$, are substantially more strongly clustered than present-day giant ellipticals. However, with the large error intervals resulting from our relatively small sample, the difference is only 2σ significance. It must also be noted that the interpretation in terms of r_0 is model-dependent. The best-fitting r_0 will be somewhat lower if Ω_m is higher or (as in the photometric $N(z)$ of Firth et al. 2002) the EROs are all at $z < 1.5$. ERO clustering is discussed further in Section 8.

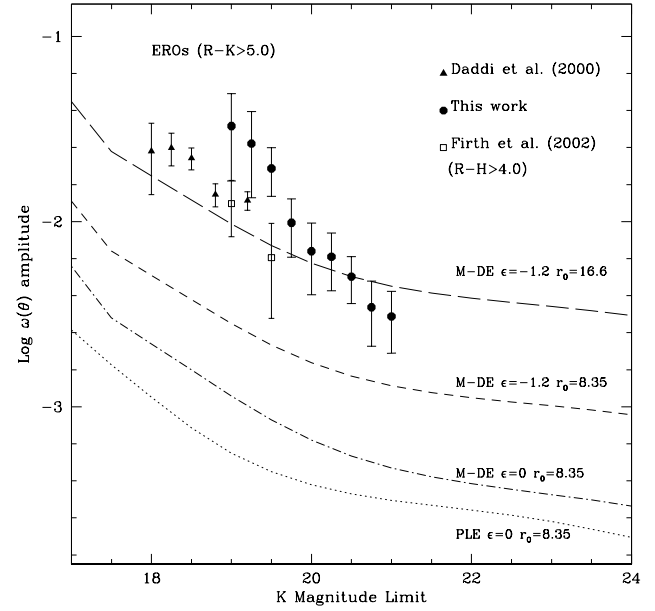


Figure 11. As Figure 10 for EROs ($R - K > 5.0$) galaxies only. The Firth et al. (2002) EROs were selected by a slightly different criterion of $R - H > 4.0$ and their H limits are converted to K limits assuming $H - K = 1$ (approximately valid for $0.8 < z < 2.6$ ellipticals). Three models with $r_0 = 8.35h_{100}^{-1}$ are plotted, PLE with $\epsilon = 0$ (dotted), M-DE with $\epsilon = 0$ (dot-dash), and M-DE with $\epsilon = -1.2$ (short dashed), plus M-DE with $\epsilon = -1.2$ and $r_0 = 16.3h_{100}^{-1}$ (long-dashed).

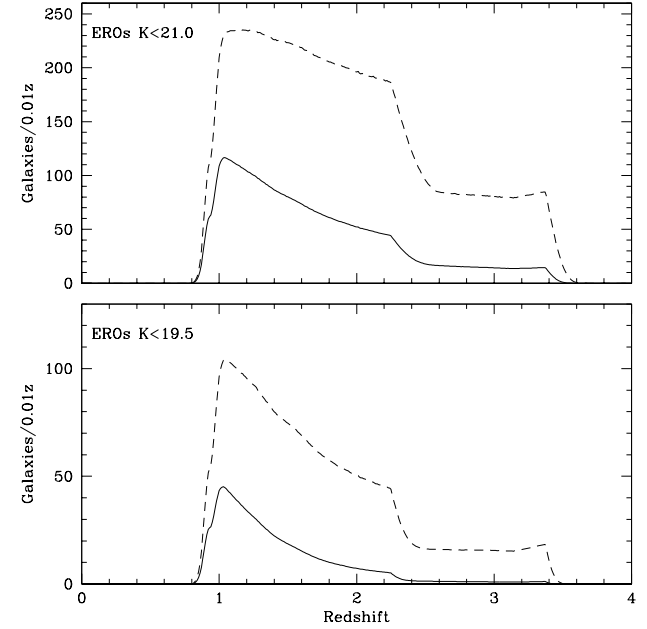


Figure 12. The redshift distribution $N(z)$ of $R - K > 5.0$ galaxies (pEROs) predicted by our PLE (dashed) and M-DE (solid) models, at limits $K \leq 19.5$ and $K \leq 21.0$.

6 MORPHOLOGY AND RADII OF EROS

6.1 Profile Fitting and Classification

We investigate the morphology and angular sizes of the EROs, to as faint a limit as possible for our ground-based data. After some experimentation, it was found that useful morphological information could be extracted from the UFTI (but not Ingrid) images of galaxies to $K \sim 19.5$. Hence, this Section concentrates on the subsample of 32 EROs on the UFTI mosaic with $K \leq 19.5$.

Table 3 gives positions and magnitudes of these objects, labelled with their detection numbers in the SExtractor catalog (prefixed ‘r’ for red). Using IRAF ‘isophote.ellipse’, we fitted a set of elliptical isophotes to the UFTI images of each of the 34 EROs, using centroids, ellipticities and position angles from the SExtractor catalog as the starting parameters. The surface brightness (SB) on each fitted isophote, as a function of semi-major axis, provides a radial intensity profile.

The aim is to estimate a morphological classification (i.e. bulge, disk or point-source) and half-light radius, r_{hl} , for each ERO, but this is greatly complicated by the need to correct for atmospheric effects. The seeing point-spread function averaged 0.67 arcsec FWHM, but with significant variation between the 16 frames of the UFTI mosaic. Hence to correct for this, for each profile fit a bright (but not saturated), relatively isolated, star was identified on the same frame as the ERO. Using IRAF ‘mkobjects’, a grid of model profiles was generated, including

- (i) a point-source,
- (ii) a set of bulge profiles,

$$I(r) = I_0 \exp\left[-7.67\left(\frac{r}{r_{hl}}\right)^{-\frac{1}{4}}\right]$$

- (iii) disk (exponential) profiles,

$$I(r) = I_0 \exp\left(-\frac{r}{r_{exp}}\right)$$

covering a wide range of r_{hl} in steps of 0.01 arcsec (for a disk profile $r_{hl} = 1.679r_{exp}$). This grid was convolved with the seeing point-spread function as represented by the star (no sky noise is added at this stage). Using ‘isophote.ellipse’, isophotal profiles were extracted from each convolved model. Each is normalized to the same total intensity as the observed ERO profile, and χ^2 -tested against it. The model giving the smallest χ^2 is (after checking the fit by eye) then adopted as the estimate for morphological type and seeing-corrected r_{hl} .

To estimate an error for r_{hl} , a second grid was generated, containing multiple copies of the normalized, best-fit model profile. This was convolved with the seeing, and noise equivalent to the sky noise added. Isophotal profiles were extracted from the resulting set of noisy models, and χ^2 tested against the observed ERO profile, and the scatter in the resulting χ^2 , $\sigma(\chi^2)$ calculated. Returning to the first grid of noiseless models, the change $\Delta(r_{hl})$ away from the best-fit model that increases the χ^2 by $\sigma(\chi^2)$ is then taken as the 1σ error on r_{hl} .

Where possible both a disk and a bulge model are fitted, so that the difference between their χ^2 , in terms of $\sigma(\chi^2)$, represents the significance by which one profile is favoured. Some EROs were not well fit by either model, but did give

a lower χ^2 when a central point-source component was included in the models. For these, point sources with flux fractions f_p were combined with bulge and disk models, and we determined the (r_{hl}, f_p) combination which minimized χ^2 . In some other EROs, the best-fit χ^2 remained large because they have ‘peculiar’ morphologies, such as a double nucleus.

6.2 Morphology: Results

Table 3 gives, for each of the 32 bright EROs, best-fit r_{hl} , ellipticity (from SExtractor), best-fit profile type and the significance by which it is favoured, and notes obvious irregularity. Figure 13 shows greyscale images of 6 of these EROs, representing a range of the morphological types, and Figure 14 shows radial intensity profiles with best-fit models.

(i) One of these EROs, r561, appears to be a pure point-source, and is probably a red Galactic star.

(ii) Of the remaining 31 EROs, 19 were best-fitted with bulge and 12 with exponential profiles. For some EROs the difference in χ^2 between the two models is very small – either they have intermediate profiles, and/or the signal/noise is insufficient for classification. Of those where one profile is favoured by $> 1\sigma$, we classify 12 as bulges and 8 as disks.

(iii) A relatively small fraction of the EROs appear to be ongoing mergers – we find 2/31. A further 6 (4 bulge, 2 disk) have some visible asymmetry, most likely from recent interactions.

(iv) The profiles of 9/31 EROs, including the ‘cluster’ ERO, r608, were better fitted with the addition of central point-source components to the underlying disk or bulge galaxies, although higher resolution data will be needed to confirm this.

In summary, the EROs at $K \leq 19.5$ appear to consist of about a 3:2 mixture of elliptical and spiral types, with about 1/4 showing evidence of ongoing or (more often) recent interactions. This is consistent with the findings of Moriondo et al. (2001) and Stiavelli and Treu (2001).

6.3 Angular Sizes of EROs

Figure 15 shows the best-fit half-light radii, r_{hl} , of the 31 (non-stellar) EROs against K magnitude, compared to models based on the radii of local galaxies. The size-luminosity relation of local E/S0s can be represented by the double power-law relation of Binggeli, Sandage and Tarengi (1984); for $M_B \leq -20$ (with $h_{50} = 1$)

$$\log(r_{hl}/\text{kpc}) = -0.3(M_B + 18.57)$$

and for $M_B > -20$

$$\log(r_{hl}/\text{kpc}) = -0.1(M_B + 15.70)$$

An E/S0 galaxy with $M_B = -21$ ($M_K = -25.04$) at $z = 0$ would, with the above size relation, have $r_{hl} = 5.36 h_{50}^{-1}$ kpc. At $z = 1$, with the luminosity evolution of our passive model, it would have $K = 18.22$, and an angular r_{hl} of 0.48 arcsec. At $z = 2$ it would appear fainter, $K = 19.44$ but little different in size, $r_{hl} = 0.46$ arcsec. Figure 15 shows the whole r_{hl} - M_B relation evolved to $z = 1$ and 2.

Table 3. Co-ordinates (equinox 2000.0) of the 32 EROs in our bright sample ($K \leq 19.5$ on UFTI image), K and R magnitudes, best-fit r_{hl} (in arcsec, with error) ellipticity $1 - \frac{b}{a}$ ($0 = \text{round}$), best-fit profile type ($d = \text{disk}$ $b = \text{bulge}$ $p = \text{point-source}$), significance $\Delta(\chi^2)$, in units $\sigma(\chi^2)$ of favouring disk or bulge, point-source fraction f_p , and other properties of morphology (*int* = in interacting pair, *dn* = double nucleus, *asn* = asymmetric – offcentre nucleus, *aso* = asymmetric outer regions, *ir* = irregular/flocculent) or emission ($X = \text{Chandra x-ray detection}$, $Ra = \text{VLA radio detection}$).

Number	R.A	Dec.	K	R	r_{hl}	ell	Type	sig	f_p	other
r91	16:36:54.32	40:56:57.43	19.084	25.655	0.35 ± 0.10	0.188	<i>b</i>	2.1	0	
r196	16:36:47.92	40:57:52.13	19.034	25.859	0.18 ± 0.04	0.128	<i>b</i>	1.03	0	
r256	16:36:48.43	40:58:08.46	18.881	25.038	0.38 ± 0.15	0.061	<i>b + p</i>	2.1	0.375	<i>Ra</i>
r270	16:36:45.13	40:58:15.69	18.843	24.625	0.28 ± 0.04	0.229	<i>b</i>	4.0	0	
r280	16:36:47.87	40:58:22.07	19.325	24.376	0.20 ± 0.03	0.171	<i>b</i>	1.05	0	
r332	16:36:50.31	40:58:42.15	19.226	24.759	0.24 ± 0.03	0.118	<i>d</i>	0.47	0	<i>asn</i>
r407	16:36:46.62	40:59:16.15	19.472	> 26	0.78 ± 0.28	0.106	<i>d + p</i>	3.3	0.6	<i>int</i>
r492	16:36:53.51	40:59:31.85	19.309	25.951	0.19 ± 0.07	0.019	<i>b + p</i>	0.38	0.5	
r506	16:36:42.77	40:59:34.36	19.410	24.997	0.31 ± 0.09	0.090	<i>b</i>	0.05	0	<i>irr</i>
r518	16:36:53.47	40:59:37.42	19.132	> 26	0.59 ± 0.18	0.230	<i>b</i>	3.1	0	<i>aso Ra</i>
r562	16:36:56.25	40:59:47.74	19.194	25.288	0.32 ± 0.04	0.039	<i>b</i>	0.05	0	<i>Ra</i>
r561	16:36:53.89	40:59:55.92	18.019	23.246	0	0.043	<i>p</i>	-	1.0	
r581	16:37:00.60	41:00:06.62	19.356	26.367	0.34 ± 0.03	0.248	<i>d</i>	0.10	0	
r585	16:36:46.19	41:00:05.93	19.131	26.950	0.40 ± 0.10	0.248	<i>b</i>	1.67	0	<i>asn</i>
r594	16:36:39.43	41:00:07.48	19.377	26.338	0.32 ± 0.10	0.210	<i>b + p</i>	0.81	0.25	<i>aso</i>
r599	16:36:45.46	41:00:10.81	19.463	25.957	0.42 ± 0.14	0.062	<i>b</i>	0.08	0	<i>asn/aso</i>
r608	16:36:57.76	41:00:21.71	17.780	23.176	0.50 ± 0.06	0.152	<i>b + p</i>	26.1	0.09	<i>X Ra</i>
r622	16:36:45.80	41:00:23.72	18.501	24.802	0.66 ± 0.05	0.325	<i>d</i>	14.8	0	<i>dn</i>
r626	16:36:58.36	41:00:25.34	19.338	25.311	0.22 ± 0.07	0.056	<i>b</i>	0.67	0	
r629	16:36:58.51	41:00:28.11	18.728	24.638	0.31 ± 0.05	0.104	<i>b</i>	2.8	0	
r642	16:36:56.99	41:00:31.76	18.610	24.819	0.32 ± 0.04	0.105	<i>b</i>	7.9	0	<i>Ra</i>
r650	16:36:38.92	41:00:33.62	18.984	24.466	0.59 ± 0.07	0.438	<i>d</i>	16.4	0	<i>irr</i>
r660	16:36:41.05	41:00:38.86	19.248	25.062	1.42 ± 0.30	0.582	<i>d</i>	12.9	0	<i>irr Ra</i>
r675	16:36:56.29	41:00:46.77	18.695	23.960	0.61 ± 0.05	0.429	<i>d</i>	> 20	0	
r852	16:36:49.75	41:01:32.89	19.222	25.575	0.28 ± 0.14	0.173	<i>b + p</i>	1.79	0.10	
r952	16:36:45.31	41:02:12.34	19.111	> 26	0.57 ± 0.08	0.351	<i>d + p</i>	> 2	0.14	<i>Ra</i>
r955	16:37:02.38	41:02:19.25	17.471	22.687	0.38 ± 0.03	0.142	<i>b</i>	17.8	0	
r1091	16:36:49.68	41:02:42.80	19.404	24.454	0.45 ± 0.10	0.057	<i>d</i>	> 10	0	
r1107	16:36:43.15	41:02:46.79	18.576	23.787	0.45 ± 0.05	0.133	<i>d + p</i>	0.9	0.12	
r1114	16:36:56.54	41:02:47.07	19.105	24.265	0.39 ± 0.19	0.150	<i>b + p</i>	0.4	0.50	
r1127	16:36:42.39	41:02:54.31	18.376	23.831	0.50 ± 0.07	0.270	<i>d</i>	1.3	0	<i>aso</i>
r1437	16:36:53.52	41:04:50.34	19.283	24.667	0.36 ± 0.06	0.156	<i>d</i>	0.02	0	

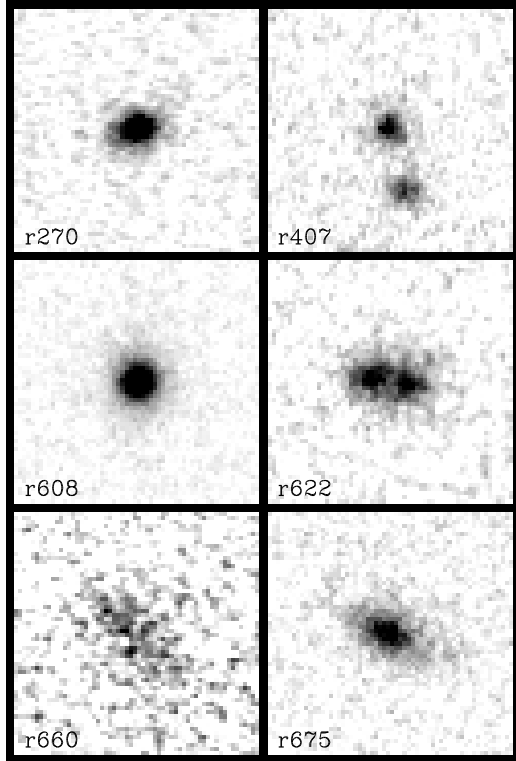


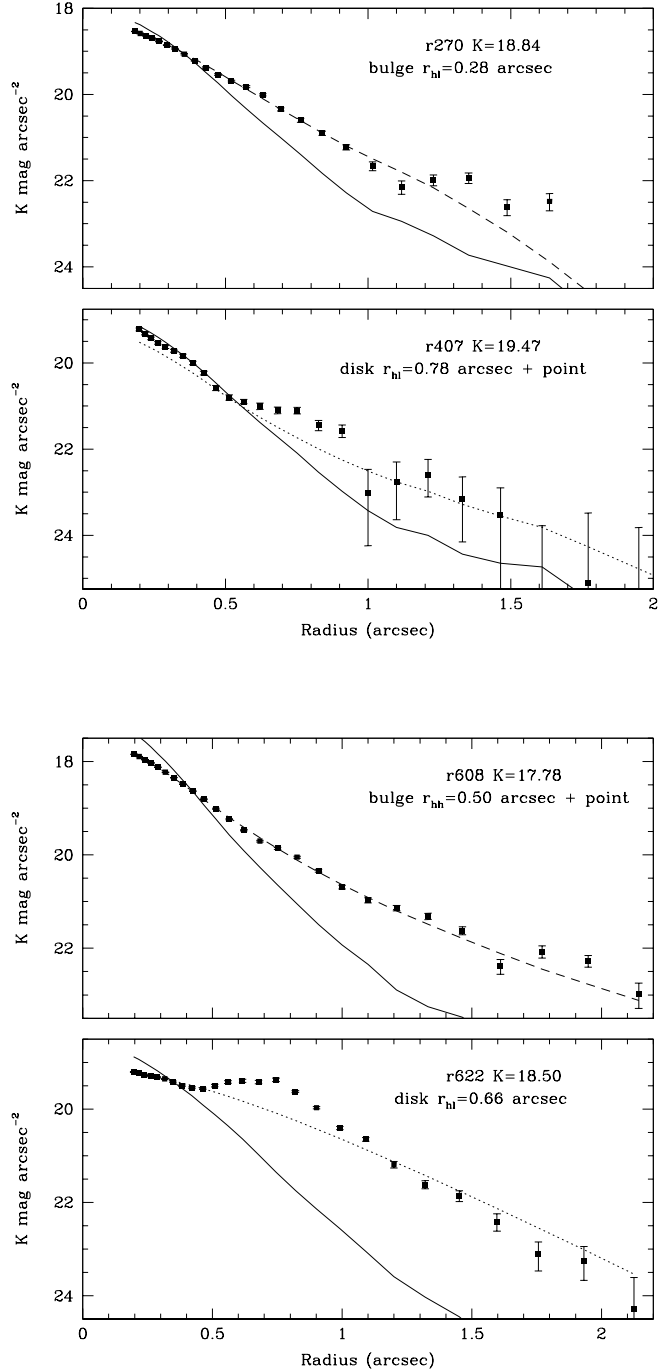
Figure 13. Greyscale K -band (UFTI) images of 6 of the brighter EROs, showing 5.45×5.45 arcsec areas. The galaxy r270 appears to be a normal elliptical, r407 a face-on disk interacting with a fainter galaxy, r608 a high-SB elliptical at the centre of a possible cluster, r622 another merging system with a double nucleus, r660 an extended, low-SB disk galaxy, and r675 an apparently regular spiral.

The brightest of these EROs, r955, has too high a surface brightness for an elliptical at $z \sim 1$. As it is also only just red enough in to have been included, the most likely explanation is that it is at a much lower redshift. However, the other 18 bulge-type EROs all have sizes consistent with passively evolving E/S0 galaxies at $0.9 < z < 2$. Most (12/19) are concentrated near the $z \sim 1$ locus with only two (r525, r612) on the $z \sim 2$ relation, as would be expected from the shape of $N(z)$ (Figure 12).

Disk EROs are more likely to be dsfEROs, and hence their surface brightness may be increased or decreased by starbursting and/or dust. Cross and Driver (2002) determine a bivariate brightness function for 45000 disk galaxies in the 2dFGRS, which gives a mean effective surface brightness $\mu_0 = 22.45 B \text{ mag arcsec}^{-2}$ at L^* ($M_B = -21.23$ for $h_{50} = 1$), with a positive correlation between surface brightness and luminosity. Their best-fit relation corresponds to

$$\log(r_{hl}/\text{kpc}) = -0.144M_B - 2.034$$

with scatter $\sigma(\log r_{hl}) = 0.103$. giving, for example $r_{hl} = 9.77h_{50}^{-1}$ kpc for $M_B = -21$, hence $0.87(0.83)$ arcsec at



$z = 1(2)$. A galaxy (of any morphology) in which star-formation is truncated long before the epoch of observation will be undergoing approximately the passive (E/S0) model luminosity evolution, so with $M_B = -21$ locally would have $K = 18.22(19.44)$ at $z = 1(2)$.

Figure 15 shows the $r_{hl} - M_B$ loci of this ‘passive disk’ model at $z = 1$ and 2. Most (10/12) of the disk EROs lie below the $z = 1$ locus, so if they are at $z \geq 1$ their intrinsic SB is greater than this model (some very dusty galaxies may be included as EROs with redshifts as low as $z \sim 0.5$ – see Figure 1). The two exceptions are the interacting r407, which lies on the $z = 2$ locus, and the very large r660, which

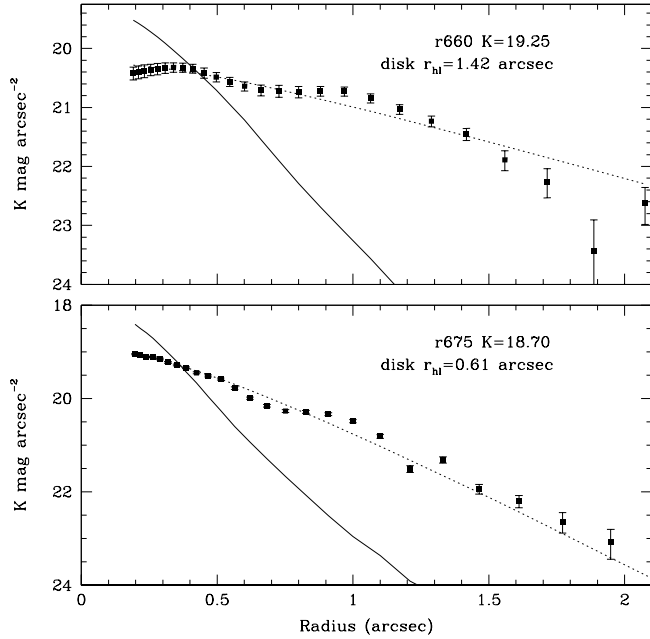


Figure 14. Radial (major axis) intensity profiles of the six EROs shown on Figure 13, compared with the best-fitting disk (dotted) or bulge (dashed) model profiles, and the point-spread function (solid line) as determined from bright stars on the same CCD frames.

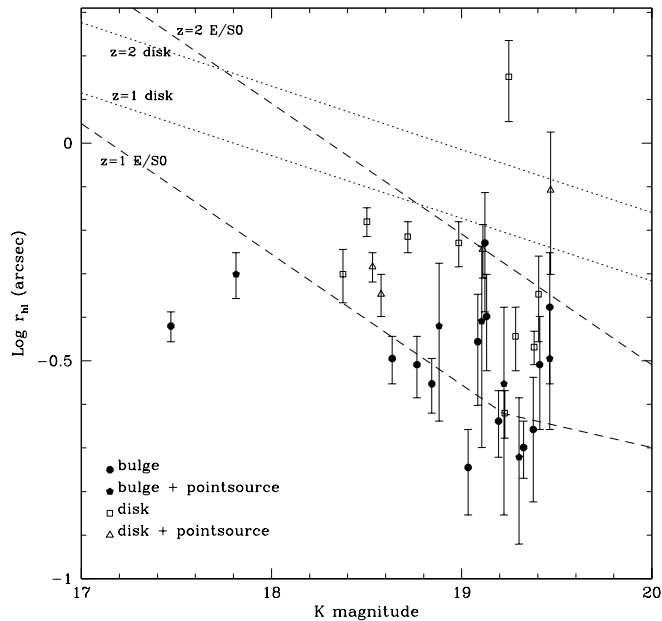


Figure 15. Half-light radii r_{hl} , as estimated by fitting radial profiles, of the 32 UFTI-field EROs with $K \leq 19.5$ (symbols indicating profile type), against K magnitude – compared with predicted sizes for E/S0 (dashed) and disk (dotted) galaxies at $z = 1$ and 2 , based on the size-luminosity relations of local E/S0s (Binggeli, Sandage and Tarenghi 1984) and spirals (Cross and Driver 2002) with passive luminosity evolution.

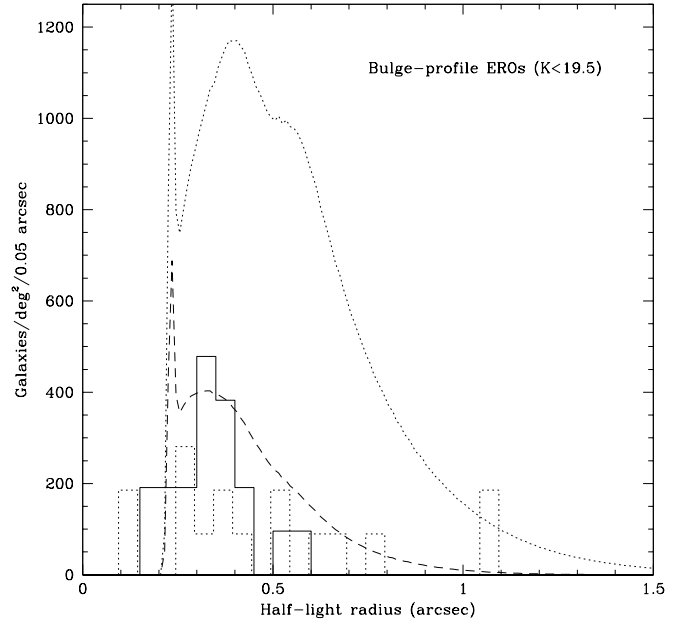


Figure 16. Angular size distribution of $K \leq 19.5$ bulge-type EROs in our sample (solid histogram), and Moriondo et al. (2000) (dotted histogram), compared to PLE (dotted) and M-DE (dashed) models.

is of a lower SB than this model, suggesting it is strongly dust-reddened (see Section 7).

Using the PLE and M-DE models, we predict r_{hl} distributions for bulge and disk EROs. Figure 16 compares the $N(r_{hl})$ of the $K \leq 19.5$ bulge-type EROs in our sample and Moriondo et al. (2000) with the models. PLE predicts $\langle z \rangle = 1.72$ and $\langle r_{hl} \rangle = 0.55$ arcsec for the bulge EROs, whereas with M-DE they are a factor 4.07 less numerous, with $\langle z \rangle = 1.42$ and $\langle r_{hl} \rangle = 0.43$ arcsec. For the 19 bulge EROs in our sample, $\langle r_{hl} \rangle = 0.33 \pm 0.03$ arcsec, but the 16 of Moriondo et al. (2000) have $\langle r_{hl} \rangle = 0.49 \pm 0.07$ arcsec (with most of the difference due to two very large cluster ellipticals), and the combined sample would be reasonably consistent with the M-DE model.

Figure 17 shows model $N(r_{hl})$ for disk-type EROs, which assume passive luminosity evolution and the spiral-type K -band luminosity function. As our models do not predict the fraction of disk EROs we have multiplied by arbitrary normalizations of 0.16 for PLE and 0.5 for M-DE. These models are compared to histograms of the 12 disk-type EROs in our sample, and the three $K \leq 19.5$ EROs from Moriondo et al. (2000) that were classed as disks. The models predict $\langle r_{hl} \rangle = 0.94$ arcsec for PLE and 0.76 arcsec for M-DE. In our sample the disk EROs tend to be smaller, $\langle r_{hl} \rangle = 0.58 \pm 0.09$ arcsec, and their modal size (see Figure 16) is similarly offset from the models.

This size discrepancy cannot simply be attributed to faster merging, as although this would shift $N(r_{hl})$ to smaller sizes, it would also reduce the ERO luminosities and hence move them rightwards along, rather than down from the $r_{hl}-M_B$ models on Figure 15. It could be due to size evolution – there is some evidence that $z > 1$ disk galaxies in

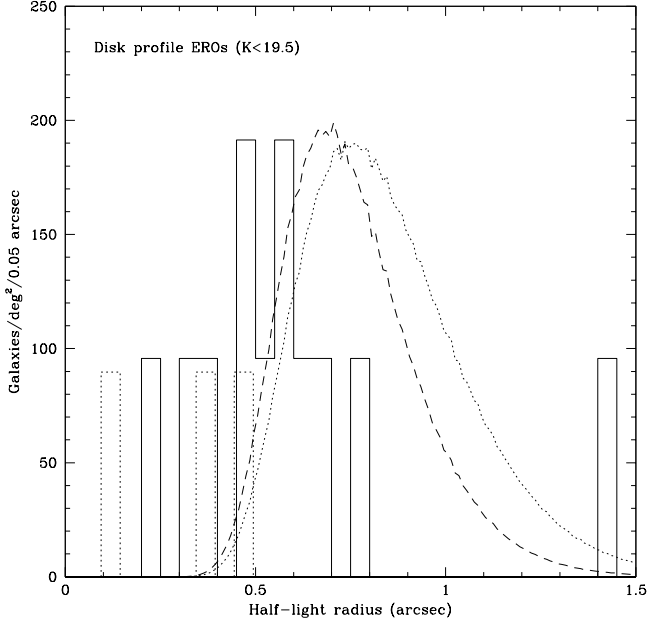


Figure 17. Angular size distribution of $K \leq 19.5$ disk-type EROs in our sample (solid histogram), and Moriondo et al. (2000) (dotted histogram); compared to PLE (dotted) and M-DE (dashed) models.

general tend to be smaller in r_{hl} than local counterparts of similar mass (Roche et al. 1997, 1998; Giallongo et al. 2000). Roche et al. (1998) hypothesised that this resulted from ‘inside-outwards’ disk formation, with the star-formation becoming more centrally concentrated at higher redshifts. Disk r_{hl} evolution appears to be quite moderate (≤ 0.1 dex) at $z \sim 1$. It is also likely that many EROs classed as disks are actually disturbed, post-interaction galaxies which may be the process of transforming into bulge galaxies, and hence have become more centrally concentrated than normal spirals.

6.4 The EROs in a possible Cluster

In Section 3.3 we noted a possible grouping of EROs centered on the X-ray and radio luminous r608. There are 11 $K < 21$ EROs within a 45 arcsec radius, of which 7 have $K \leq 19.5$ – r552, r581, r608, r626, r629, r642, and r675, an overdensity compared to the 1.6 $K \leq 19.5$ EROs expected by chance in this area. If the EROs in this area belong to a single cluster, they should trace an iso-redshift locus on the $r_{hl} - K$ plot. We see (Figure 18) that the five bulge-type EROs lie neatly on the $z = 1$ E/S0 locus, and the two disks are 0.1–0.2 dex below the $z = 1$ disk model. If these disks have a similar size offset from this model as the distribution on Figure 16, these radii are entirely consistent with all 7 EROs belonging to a single, $z \sim 1$ cluster. Of course, to confirm this will require spectroscopic redshifts (which we plan to obtain).

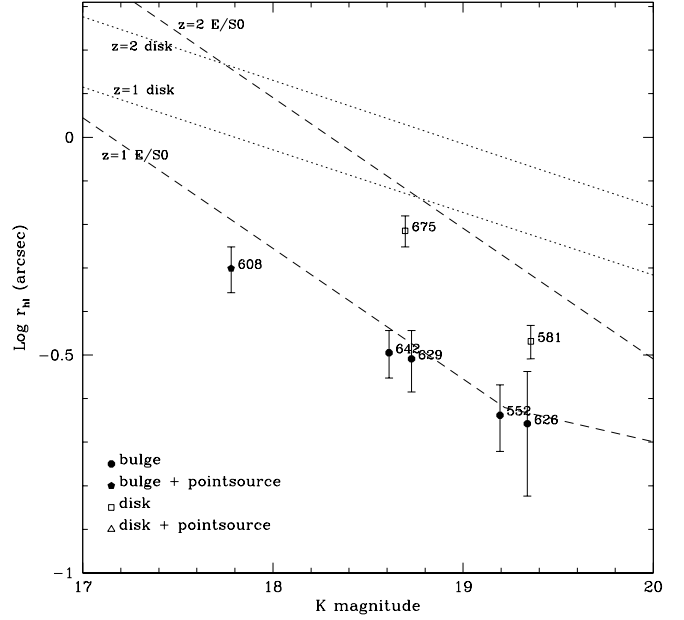


Figure 18. Half-light radii r_{hl} , as estimated by fitting radial profiles, of the 7 EROs with $K \leq 19.5$ within a 45 arcsec radius of r608, against K magnitude. Galaxies are labelled with detection numbers, with symbols indicating profile type. The plotted models are as in Figure 15.

Table 4. Radio and/or X-ray fluxes of the seven $K \leq 19.5$ UFTI subsample EROs detected in the VLA and/or Chandra surveys.

ERO	$F(1.4 \text{ GHz})$ (μJy)		$F(0.5\text{--}8.0 \text{ keV})$
	peak	integral	$10^{-15} \text{ ergs s}^{-1} \text{ cm}^{-2}$
r256	32.4 ± 9.5	25.1 ± 13.9	-
r518	27.7 ± 9.5	30.0 ± 17.3	-
r552	39.3 ± 9.5	21.8 ± 11.3	-
r608	$4477. \pm 9.5$	$5074. \pm 17.8$	3.060 ± 0.891
r642	58.3 ± 9.5	46.7 ± 14.2	-
r660	29.1 ± 9.3	39.3 ± 19.8	-
r952	48.0 ± 9.5	43.4 ± 15.4	-

7 RADIO, X-RAY AND SUB-MM OBSERVATIONS

The ELAIS N2 field has also been observed:

(i) At radio (1.4 GHz) frequencies using the VLA, reaching a 3σ threshold for source detection $F(1.4 \text{ GHz}) \simeq 27.6 \mu\text{Jy}$, with resolution 1.4 arcsec (see Ivison et al. 2002).

(ii) In X-rays using the Chandra satellite, for 75 ks in August 2000, reaching source detection limits $F(0.5\text{--}8.0 \text{ keV}) \simeq 1.5 \times 10^{-15} \text{ ergs s}^{-1} \text{ cm}^{-2}$ with sub-arcsec resolution (Manners et al. 2002).

(iii) At $850 \mu\text{m}$ using SCUBA, reaching a 3.5σ source detection limit of $F(850 \mu\text{m}) \simeq 8 \text{ mJy}$ (Scott et al. 2002).

Here we discuss these observations for the $K \leq 19.5$ UFTI EROs only. Seven of these 31 galaxies are detected at 1.4 GHz sources, only one as an X-ray source, and none in the sub-mm. Table 4 gives the fluxes of the detections. In r256, r518, r552, r642 and r952, the radio emission is rela-

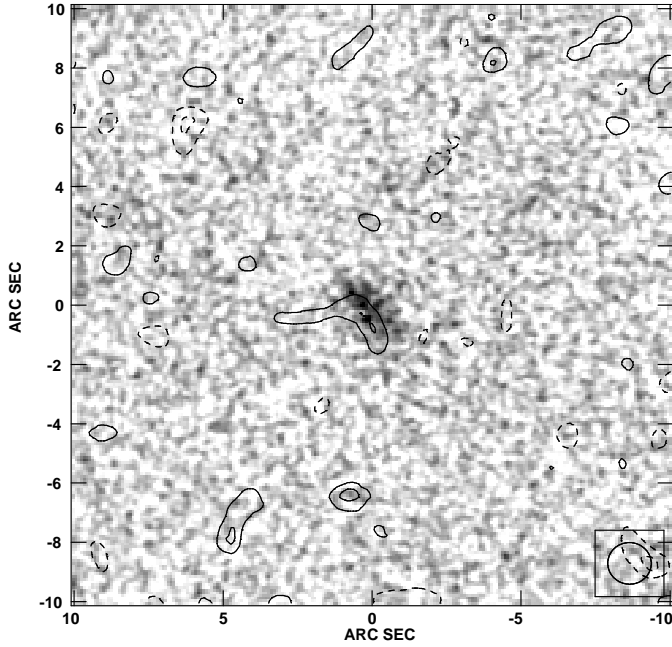


Figure 19. Radio contour map centred on r660, generated from VLA data using the AIPS package, superimposed on the UFTI *K*-band image. The radio contours are at 2 and 3 σ where $\sigma = 9.2\mu\text{Jy}/\text{beam}$ (dotted contours are negative).

tively weak and consistent with a point source, and the host galaxies appear to be regular ellipticals (the outer regions of r518 are mildly disturbed). The radio emission is stronger than would be expected for typical L^* ellipticals ($< 10\mu\text{Jy}$ at all $z > 1$) and seems more likely to be produced by weak AGN, below the Chandra threshold, rather than powerful starbursts.

The galaxy r660, similar to these five in radio flux, differs in that (i) the radio emission is elongated, with major axis FWHM ~ 2.3 arcsec on a position angle 27 ± 18 degrees, and (as shown on Figure 19) aligned with the *K*-band long axis, (ii) the galaxy is a large low-surface brightness disk. This suggests that the radio emission is produced by an extended dust-reddened starburst. With the Condon (1992) radio SED, the $39.3\mu\text{Jy}$ flux corresponds to a rest-frame luminosity (νL_ν) at $z = 1(2)$ of $L_{1.4} = 10^{39.66}(10^{40.34})h_{50}^{-2}$ ergs s^{-1} . If $L_{1.4}/\text{SFR}$ is in the range bracketed by the Carilli (2000) and Condon (1992) relations, as in Roche et al. (2002), the total SFR = $99\text{--}233(474\text{--}1115)h_{50}^{-2} M_\odot\text{yr}^{-1}$ at $z = 1(2)$, and r660 is a very powerful starburst galaxy, probably similar to local ULIRGs.

The non-detection of any of these 31 EROs in the SCUBA survey sets an upper limit on their SFR. Scott et al. (2002) estimate the detection limit of $F(850\mu\text{m}) \simeq 8\text{mJy}$ to correspond to a SFR $\sim 1800h_{50}^{-2} M_\odot\text{yr}^{-1}$, at all $1 < z < 10$, for the Salpeter IMF, which for the IMF of our models becomes $\sim 1200h_{50}^{-2} M_\odot\text{yr}^{-1}$. Most of these bright EROs, including the double nucleus and disturbed galaxies, are not detected in the VLA data either, which sets stricter upper limits on SFRs, $\simeq 70\text{--}164(335\text{--}785)h_{50}^{-2} M_\odot\text{yr}^{-1}$ at $z = 1(2)$. As most of the brightest EROs will be closer to $z \sim 1$, this implies that the average SFR of dsfEROs at these redshifts is less than $\sim 200h_{50}^{-2} M_\odot\text{yr}^{-1}$. Nevertheless, a significant

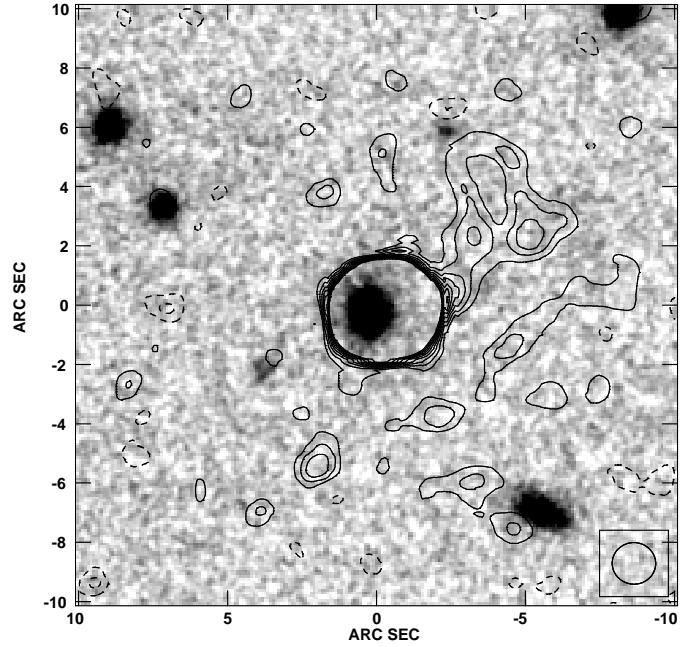


Figure 20. Radio contour map centred on r608, superimposed on the UFTI *K*-band image. The radio contours are at 2,3,4...10 σ where $\sigma = 9.2\mu\text{Jy}/\text{beam}$.

minority – e.g. r660, and the numerous examples of fainter EROs associated with SCUBA sources (Smail et al. 1999; Dey et al. 1999; Ivison et al. 2001; Lutz et al. 2001) – are real ULIRGs.

By far the strongest radio source in this sample, at 5mJy , is r608, the X-ray source and possible cluster central galaxy. The X-ray and VLA data (Figure 20) show most of the emission from a point-source concentric with the *K*-band profile. The radio flux is far too strong to be attributed to star-formation (the non-detection with SCUBA limits the starburst contribution to ≤ 1 per cent of this). If r623 is at $z \simeq 1$, the rest-frame radio luminosity, $L_{1.4} \simeq 10^{41.75}$ ergs s^{-1} . This is 3 orders of magnitude above that of normal spirals but 3 orders below the most powerful radio galaxies. If we assume passive optical evolution and $(1+z)^3$ radio evolution for this galaxy then at $z = 0$ it would have $M_R = -23.24$ and $L_{1.4} \simeq 10^{40.85}$ ergs s^{-1} , or $P_{1.4} = 10^{24.70}$ W Hz^{-1} , and its position on the radio-optical luminosity plane (Ledlow and Owen 1996) would then be typical of local FRI radio galaxies.

The X-ray flux, $F(0.5\text{--}8.0 \text{ keV}) = 3.06 \times 10^{-15}$ ergs $\text{s}^{-1}\text{cm}^{-2}$, corresponds at $z \simeq 1$, assuming a $f_\nu \propto \nu^{-1}$ spectrum, to $L_X(0.5\text{--}8.0\text{keV}) = 10^{43.50}$ ergs s^{-1} , which could also be expressed in the νL_ν form as $L_{1\text{keV}} = 10^{43.27}$ ergs s^{-1} . From this, the radio to X-ray spectral index, $\alpha_{RX} \simeq \frac{41.75 - 43.27 + 8.24}{8.24} = 0.815$, which is also consistent with an FRI radio galaxy (e.g. Capetti et al. 2002).

8 SUMMARY AND DISCUSSION

8.1 Summary

(i) The number counts of ERO galaxies are lower than predicted if a PLE model is assumed for all local E/S0s, but

much higher than the hierarchical merging models (Cimatti 2002b). The ERO counts could be fitted by an ‘M-DE’ model, in which some giant ellipticals do form at high redshifts but both the characteristic mass and the comoving number density of passively evolving galaxies decrease with redshift. Physically this could be explained by a continual process of galaxy merging and other interactions in which some of the red ellipticals are formed from star-forming spirals.

The ‘M-DE’ model best-fitting our ERO counts includes the observed merger rate and evolution (Patton et al. 2001), with the additional parameter $R_\phi = -0.46$, meaning that only ~ 35 per cent of the present-day comoving number density of E/S0 galaxies formed at $z > 3$. This fraction is higher than the ~ 15 per cent estimated by Stiavalli and Treu (2001), because we have (a) included all types of ERO as possible E/S0 progenitors (b) included the effects of merging in reducing mean mass and hence L^* at high redshift, thus allowing a higher number density of passive galaxies.

(ii) We examined the morphology of a bright ($K < 19.5$) subsample of 32 EROs on the UFTI mosaic. One appeared to be a Galactic star, the other 31 a $\sim 3:2$ mixture of elliptical and disk profile types. About 1/4 showed some evidence of asymmetry or disturbance, e.g. from recent interactions, but only two were obvious mergers with double nuclei. This mixture of morphologies is consistent with the findings of Moriondo et al. (2001) and Stiavelli and Treu (2001) for similar samples of EROs.

By fitting radial profiles, we estimated seeing-corrected half-light radii. The r_{hl} of the bulge-type EROs were consistent with passively evolving E/S0 galaxies in the redshift range ($0.9 < z < 2.0$) predicted by the M-DE model. This is in agreement with Moriondo et al. (2000) who found the surface brightness–size relation of six bulge-type EROs at known redshifts of $z \sim 1.3$ to be consistent with passively evolved ($\Delta(B) = -1.4$ mag) 1 ellipticals. However, larger samples and higher resolution data (e.g. HST imaging) will be needed before ERO radii can place strong constraints on merging models. The r_{hl} of the disk-profile EROs are on average smaller than expected for passively evolved spirals. Possible explanations include size and/or morphological evolution.

(iii) Radio observations with the VLA detect emission above the 3σ limit of $F(1.4 \text{ GHz}) \simeq 27.6 \mu\text{Jy}$ for 7 of the 31 ERO galaxies with $K < 19.5$ on the UFTI field. The strongest of these sources, at 5 mJy, would be a radio galaxy, perhaps like local FRIs if these evolve as strongly as $L_{rad} \propto (1+z)^3$. The host galaxy is also a Chandra X-ray source and our data suggests it may be the central giant elliptical of a cluster of EROs. Of the other, much fainter ($30\text{--}60 \mu\text{Jy}$) detections, five are point sources within apparently regular galaxies, and may be weak AGN. The seventh, the galaxy r660, shows elongated radio emission aligned with the K -band image. The galaxy is a large disk of lower surface brightness than the other bright EROs. These properties suggest it is a powerful but very dust-reddened starburst, with a SFR $100\text{--}1000 h_{50}^{-2} M_\odot \text{yr}^{-1}$.

The non-detection of the other EROs, which include double-nucleus and disturbed objects, implies their SFRs are lower. This was interpreted as indicating the mean SFR

of the dsfEROs to be $< 200 h_{50}^{-2} M_\odot \text{yr}^{-1}$. This is probably consistent with the Cimatti et al. (2002a) estimate of $\sim 100 h_{50}^{-2} M_\odot \text{yr}^{-1}$, based on the mean [OII]3727 and UV fluxes of spectroscopically observed dsfEROs (see 8.2 below), after correcting for $E(B-V) = 0.5$ mag extinction.

(iv) We investigated the angular correlation function $\omega(\theta)$ of EROs on the UFTI+Ingrid fields and two EIS-Deep survey fields. Positive clustering is detected for the EROs at the $\sim 3\sigma$ level, and their $\omega(\theta)$ amplitude appears to be almost an order of magnitude higher than that of all galaxies to the same K mag limits. For the $N(z)$ given by our M-DE model, with $\Omega_m = 0.3$, $\Lambda = 0.7$ and comoving clustering, our $\omega(\theta)$ amplitudes for EROs were best fitted with a correlation radius of $r_0 \simeq 16.6 \pm 3.7 h_{100}^{-1} \text{ Mpc}$. This model is also consistent with the ERO clustering of Daddi et al. (2000) and Firth et al. (2002) at brighter limits, but the large statistical uncertainties will require the analysis to be repeated with much larger samples of EROs.

8.2 Discussion

8.2.1 Star-forming EROs

Cimatti et al. (2002a), using VLT spectroscopy, classified the spectra of about two-thirds of a sample of bright ($K \leq 19.2$) EROs, and found approximately half (50 ± 17 per cent) to be dusty star-forming and half to be old (> 3 Gyr) passive galaxies. The averaged spectrum of the dsfEROs showed [OII]3727 emission and Balmer absorption lines and closely resembled an e(a) type (Poggianti and Wu 2000) ‘very luminous infra-red galaxy’ with stellar reddening $E(B-V) \sim 0.5$.

The VLA data indicate that only a small fraction of EROs can be ULIRGs, and furthermore the proportion of EROs which are ongoing mergers or very disturbed is considerably lower than 50 per cent, so some dsfEROs must have more regular bulge or intermediate profiles. This suggests that many of the dsfEROs are in late post-merger stages, with low and declining SFR and increasingly regular morphology. These galaxies may subsequently become E/S0s and contribute to the increase with time in the comoving number density of passive galaxies. The dsfEROs and pEROs would then be separate stages of an evolutionary sequence. At $z \sim 1\text{--}2$ we see the second (pERO) stage for the earliest formed ellipticals, contemporaneous with the dsfERO stage of those forming later, while deeper ERO surveys would reach the dusty starburst phase of the first massive ellipticals, at $z \geq 3$ (i.e. the SCUBA sources).

On the basis of the Cimatti et al. (2002a) spectroscopy, dsfEROs would make up $\sim (0.5 \pm 0.17) \times 14 = 7 \pm 2$ per cent of all $K \leq 20$ galaxies and to this limit have a surface density $0.69 \pm 0.23 \text{ arcmin}^{-2}$. These high numbers imply the dsfERO phase is prolonged. For an order-of-magnitude estimate of the total dsfERO lifetime, t_{dsf} , we assume that (i) each present-day E/S0 galaxy is associated with an average of one dsfERO ‘event’ at higher redshift, (ii) that the K -band magnitudes of dsfEROs can be approximated by the passive model with merging (as they seem to be similar in surface brightness to the pEROs).

If t_{dsf} lasted for the entire ‘ERO epoch’, $z > 0.93$, the dsfERO count might then be represented by the $z > 0.93$

galaxies in a model for E/SOs with merging ($R_m = 0.3$) but no change in comoving number density, $R_\phi = 0$. This would be intermediate between the merging and M-DE models on Figure 6 and to $K = 20$ gives 2.9 arcmin^{-2} . Most $K \leq 20$ EROs will be at $0.93 < z < 2$, or lookback times $(10.4\text{--}14.4)h_{50}^{-1} \text{ Gyr}$, hence $t_{dsf} \sim \frac{0.69}{2.3} \times (14.4 - 10.4) = 1.2h_{50}^{-1} \text{ Gyr}$.

8.2.2 Clustering and evolution

We estimate the intrinsic clustering of EROs as $r_0 = 16.6 \pm 3.7h_{100}^{-1} \text{ Mpc}$ comoving, which is considerably stronger than for present-day giant ellipticals. Hence if the EROs at $z \sim 1\text{--}2$ evolve into the present-day E/SOs, the increase in their comoving number density over the same redshift interval must be accomplished primarily by the ‘assimilation’ of less clustered types of galaxy, reducing the r_0 .

It may be significant that Abell galaxy clusters are even more strongly clustered, with $r_0 \simeq 21h_{100}^{-1} \text{ Mpc}$ (Abadi, Lambas and Muriel 1998), and there are preliminary indications that SCUBA sources are at least as intrinsically clustered as EROs (Almaini et al. 2002). The Lyman break galaxies at $z \sim 3$ may be very diverse but on the whole are more moderately clustered, with comoving $r_0 \simeq 3\text{--}4h_{100}^{-1} \text{ Mpc}$ (Arnouts et al. 2001), suggesting they are mostly progenitors of disk galaxies.

Daddi et al. (2002) find some evidence (based on a small sample of redshifts) that the strong clustering of EROs is associated with the pERO types only, and estimate $r_0 < 2.5h_{100}^{-1} \text{ Mpc}$ for dsfEROs. They argue that this may be evidence against dsfEROs being E/SO progenitors.

However, this difference in clustering is as expected if (i) the oldest EROs (i.e. the pEROs) form at very dense mass concentrations, which are the ‘seeds’ of Abell clusters and SCUBA sources and hence are similarly clustered, and (ii) the addition of dsfEROs (formed from mergers of the weakly clustered disk galaxies) to the ERO class produces a continual dilution of the clustering until, by $z \sim 0$, the passive galaxy r_0 is that observed for local E/SOs. Secondly, the IRAS ($60\mu\text{m}$) sources, which may be low redshift counterparts of the dsfEROs, are weakly clustered ($r_0 \simeq 4h_{100}^{-1} \text{ Mpc}$), but nevertheless have many properties suggesting they are destined to evolve into ‘disky’ E/SOs (Genzel et al. 2001).

Thirdly, many low-redshift E/SO are observed to have ‘boxy’ or ‘disky’ isophotes, and this may be ‘fossil’ evidence that they evolved from both types of ERO. The ‘boxy’ ellipticals tend to be more massive and more confined to the centres of clusters, with slightly older stellar populations. The ‘disky’ galaxies tend to have higher rotation velocities (v_{rot}) but lower internal velocity dispersions (σ_i).

These differences may result from the ‘disky’ ellipticals having formed at a relatively late epoch when large spirals were already present, perhaps (at one extreme) from the merger of a single pair of spirals. This would probably impart a substantial angular momentum to the post-merger. At the other extreme, the formation of the oldest ellipticals may occur through the multiple merger of a much larger number of small disks in the core of a proto-cluster, this giving a summed angular momentum vector much closer to zero, and ‘boxy’ isophotes. This latter process may have been observed in deep K images of high- z radio galaxies, which show

massive ellipticals at $z < 3$ but a large number of clustered sub-components at $z > 3$ (van Breugel et al. 1999).

At $z \sim 1\text{--}2$, the progenitors of today’s ‘boxy’ and ‘disky’ E/SOs would then be, respectively, the pEROs and dsfEROs.

8.2.3 Future plans

We hope to investigate these scenarios further through

(i) analysing the clustering of much larger samples of EROs, ideally with multi-colour imaging (e.g. R , J , H and K) to enable separation of the dsfEROs and pEROs. It may be especially useful to compare the clustering properties of EROs and SCUBA sources.

(ii) High-resolution spectroscopy of a diverse sample of EROs, with the aim of age-dating their stellar populations, as well as estimating current SFR, internal dust extinction, metallicity and kinematics. The velocities σ_i and v_{rot} can be measured from ground-based spectroscopy, even at high redshifts. Using a $v_{rot}\text{--}\sigma_i$ plot (Genzel et al. 2001), the ERO progenitors of ‘disky’ and ‘boxy’ ellipticals might then be identified.

Acknowledgements

This paper is based on observations with the WHT and UKIRT. The William Herschel Telescope is operated on the island of La Palma by the Isaac Newton Group in the Observatorio del Roque de los Muchachos of the Instituto de Astrofísica de Canarias. The United Kingdom Infrared Telescope is operated by the Joint Astronomy Centre on behalf of the UK Particle Physics and Astronomy Research Council. NR acknowledges the support of a PPARC Research Associateship. OA acknowledges the support of a Royal Society Research Fellowship. JSD acknowledges the support of a PPARC Senior Fellowship. CJW and RJI thank PPARC for support. We make use of some catalog data from EIS-DEEP, for which observations have been carried out using the ESO New Technology Telescope (NTT) at the La Silla observatory under Program-ID Nos. 61.A-9005(A), 162.O-0917, 163.O-0740, 164.O-0561.

REFERENCES

- Abadi M., Lambas D., Muriel H., 1998, ApJ, 507, 526.
- Almaini O., et al., 2002, MNRAS, in press.
- Barger A., Cowie L., Trentham N., Fulton E., Hu E.M., Songaila A., Hall D., 1999, AJ, 117, 102.
- Bertin E., Arnouts S. 1996, A&AS, 117, 393.
- Cabanac A., de Lapparent V., Hickson P., 2000, A&A, 364, 349.
- Capetti A., Celotti A., Chiaberge M., de Ruiter H.R., Fanti R., Morganti R., Parma, P, 2002, A&A, 383, 104.
- Carilli C., Bertoldi F., Omont A., Cox P., McMahon R., Isaak K., 2001, AJ, 122, 1679.
- Cimatti A., et al., 2002a, A&A, 381, 68.
- Cimatti A., 2002b, ‘The Mass of Galaxies at Low and High Redshift’, proceedings of ESO/USM workshop (astro-ph/0201050).
- Condon J.J., 1992, A&A Ann. Rev., 30, 575.
- Cross N., Driver S., 2002, MNRAS, 329, 579.
- Daddi E., Cimatti A., Pozzetti L., Hoekstra H., Röttgering, H., Renzini A., Zamorani G., Mannucci F, 2000, A&A, 361, 535.
- Daddi E., et al., 2002, A&A, 384, 1.

- Dey A., Graham J., Ivison, R.J., Smail I., Wright G., Liu M., 1999, *ApJ*, 519, 610.
- Dunlop J., Peacock J., Spinrad H., Dey A., Jimenez R., Stern D., Windhorst R., 1996, *Nature*, 381, 581.
- Elston R., Rieke M., Rieke G., 1988, *ApJ*, 331, L77.
- Fioc M., Rocca-Volmerange B., 1997, *A&A*, 326, 950.
- Firth A.E., et al., 2002, *MNRAS*, 332, 617.
- Genzel R., Tacconi L., Rigopoulou D., Lutz D., Tecza M., 563, 527.
- Giallongo E., Menci N., Poli F., D'Odorico S., Fontana A., 2000, *ApJ*, 530, L73.
- González-Solares E., et al., 2002, in prep.
- Guzzo L., Strauss M., Fisher K., Giovanelli R., Haynes, M., 1997, *ApJ*, 489, 37.
- Hu E.M., Ridgeway S.E., 1994, *AJ*, 107, 1303.
- Ivison, R.J., Dunlop J.S., Smail I., Dey A., Liu M., Graham J., *ApJ*, 542, 27.
- Ivison R.J., et al., 2002, in prep?
- Jimenez R., Friaca A. S., Dunlop J.S., Terlevich R., Peacock, J., Nolan L., 1999, *MNRAS*, 305, L16.
- Kochanek C., et al., 2001, *ApJ*, 560, 566.
- Kuemmel W., Wagner J., 2000, *A&A*, 353, 867.
- Ledlow, M., Owen, F., 1996, *AJ*, 112, 9.
- Lutz D, et al., 2001, *A&A*, 378, 70.
- Manners J., et al., 2002, in prep.?
- Mannucci F., Pozzetti L., Thompson D., Oliva E., Baffa C., Comoretto G., Gennari S., Lisi F., 2002, *MNRAS*, 329.
- McCracken H., Shanks T., Metcalfe N., Fong R., Campos A., 2000, *MNRAS*, 318, 913.
- Moustakas L., Davis M., Graham J., Silk J., Peterson B., Yoshii Y., *ApJ*, 475, 445.
- Moriondo G., Cimatti A., Daddi E., 2000, *A&A*, 364, 26.
- Oliver S., et al., 2000, 316, 749.
- Patton D., et al., 2002, *ApJ*, 565, 208.
- Poggianti B., Wu H., 2000, *ApJ*, 529, 157.
- Roche N., Lowenthal J., Koo D., 2002, *MNRAS*, 330, 307.
- Roche N., Eales S., 1999, *MNRAS*, 307, 703.
- Roche N., Ratnatunga K., Griffiths R.E., Im M., Naim A., 1998, *MNRAS*, 293, 157.
- Roche N., Ratnatunga K., Griffiths R.E., Im M., 1997, *MNRAS*, 288, 200.
- Saracco P., Giallongo E., Cristiani S., D'Odorico S., Fontana A., Iovino A., Poli F., Vanzella E., 2001, *A&A*, 375, 2001.
- Scott S., et al., 2002, *MNRAS*, submitted (astro-ph/107446).
- Smail I., Ivison R.J., Kneib J.-P., Cowie L., Blain A., Barger A., Owen F., Morrison G., *MNRAS*, 1999, 308, 1061.
- Smith G., Treu T., Ellis R., Smail I., Kneib J.-P., Frye B., 2001, *ApJ*, 562, 635.
- Smith G., et al., 2002, *MNRAS*, 330, 1.
- Spinrad H., Dey A., Stern D., Dunlop J., Peacock J., Jimenez R., Windhorst R., 1997, *ApJ*, 484, 581.
- Stanford S., Elston R., Eisenhardt P., Spinrad H., Stern, D., Dey A., 1997, *AJ* 114, 2232.
- Stiavelli M., Treu T., 2001, 'Galaxy Disks and Disk Galaxies', *ASP Conf. Series.*, vol. 230, 603.
- van Breugel W., Stanford S., Spinrad H., Stern D., Graham J., 1998, *ApJ*, 502, 614.